



Galactic Bar Resonances with Diffusion: An Analytic Model with Implications for Bar–Dark Matter Halo Dynamical Friction

Chris Hamilton¹ , Elizabeth A. Tolman^{1,2} , Lev Arzamasskiy¹ , and Vinícius N. Duarte³ ¹ Institute for Advanced Study, Einstein Drive, Princeton, NJ 08540, USA; chamilton@ias.edu
² Center for Computational Astrophysics, Flatiron Institute, 162 Fifth Avenue, New York, NY 10010, USA
³ Princeton Plasma Physics Laboratory, Princeton University, Princeton, NJ 08543, USA

Received 2022 August 9; revised 2023 May 15; accepted 2023 May 16; published 2023 August 18

Abstract

The secular evolution of disk galaxies is largely driven by resonances between the orbits of “particles” (stars or dark matter) and the rotation of non-axisymmetric features (spiral arms or a bar). Such resonances may also explain kinematic and photometric features observed in the Milky Way and external galaxies. In simplified cases, these resonant interactions are well understood: for instance, the dynamics of a test particle trapped near a resonance of a steadily rotating bar is easily analyzed using the angle-action tools pioneered by Binney, Monari, and others. However, such treatments do not address the stochasticity and messiness inherent to real galaxies—effects that have, with few exceptions, been previously explored only with complex N -body simulations. In this paper, we propose a simple kinetic equation describing the distribution function of particles near an orbital resonance with a rigidly rotating bar, allowing for diffusion of the particles’ slow actions. We solve this equation for various values of the dimensionless diffusion strength Δ , and then apply our theory to the calculation of bar–halo dynamical friction. For $\Delta = 0$, we recover the classic result of Tremaine and Weinberg that friction ultimately vanishes, owing to the phase mixing of resonant orbits. However, for $\Delta > 0$, we find that diffusion suppresses phase mixing, leading to a finite torque. Our results suggest that stochasticity—be it physical or numerical—tends to increase bar–halo friction, and that bars in cosmological simulations might experience significant artificial slowdown, even if the numerical two-body relaxation time is much longer than a Hubble time.

Unified Astronomy Thesaurus concepts: Galactic bar (2365); Barred spiral galaxies (136); Galaxy dark matter halos (1880); Dynamical friction (422); Orbital resonances (1181); Stellar kinematics (1608); Plasma physics (2089)

1. Introduction

Galaxies are sculpted by resonances. Corotation, Lindblad, and ultraharmonic resonances of rotating non-axisymmetries like bars and spirals are likely responsible for disk heating, radial migration, and mixing in the Milky Way (Binney & Lacey 1988; Sellwood & Binney 2002; Roškar et al. 2008; Schönrich & Binney 2009; Minchev et al. 2012; Sridhar 2019); for the formation of solar neighborhood moving groups (Dehnen 2000; Hunt et al. 2019; Kawata et al. 2021); and for producing the rings and dark gaps observed in external galaxies (Buta 1986, 2017; Krishnarao et al. 2022). The (in)stability of self-gravitating oscillation modes is dictated by the number of stars or dark matter particles that are able to resonate with the mode and hence transfer angular momentum to/from it (Palmer & Papaloizou 1987; Weinberg 1994; Sellwood 2014; Rozier 2020). Orbital resonances between stars in galactic disks, amplified by collective effects, drive rapid relaxation of the stellar distribution function (DF; Sellwood 2012; Fouvry et al. 2015). The infall of heavy satellites and slowing of galactic bars is likely driven by dynamical friction due to the resonant trapping of dark matter particles (Lynden-Bell & Kalnajs 1972; Tremaine & Weinberg 1984; Kaur & Sridhar 2018; Banik & van den Bosch 2021; Chiba & Schönrich 2021). Thus, the study of secular evolution of galaxies is in large part the study of resonant dynamics; to quote from Weinberg & Katz (2007a), “resonances are not the exception but are required for galaxy evolution!”

The existence of resonant structures in galaxies is an inevitable consequence of the quasiperiodicity of most stellar/dark matter orbits in the mean galactic potential. Given this quasiperiodicity, resonant interactions are often best described in angle-action coordinates. Binney (2012, 2016, 2018, 2020a, 2020b) has pioneered the use of these coordinates to construct analytic equilibrium galaxy models, and to calculate the distribution function (DF) of resonantly trapped stars. In the latter case, one assumes that the galactic potential consists of an axisymmetric mean field plus a rigidly rotating non-axisymmetric perturbation (see also Monari et al. 2016, 2017, 2019). An alternative way to capture the same physics is to integrate numerically the orbits of an ensemble of test particles in this prescribed potential (e.g., Hunt et al. 2019; Sellwood et al. 2019). As a result of such efforts, resonances are now often employed in galactic dynamics as diagnostic tools—reliable dynamical features whose imprints tell us something about the underlying galaxy. For instance, several authors have attempted to infer the size and pattern speed of the Milky Way’s bar by fitting test particle models of its resonant imprint to solar neighborhood kinematic data (Dehnen 2000; Antoja et al. 2014; Trick et al. 2019; Trick 2021). Even more ambitiously, Chiba et al. (2020) and Chiba & Schönrich (2021) have suggested one might retrace the history of the Galactic bar’s pattern speed by identifying a “tree ring” structure in the kinematics of resonantly trapped stars. Again, the analytic and numerical tools for this analysis treated the stars as test particles under the influence of a rigidly rotating perturbation. A crucial element missing from these models is the diffusion of the particles in question, due to stochasticity in the gravitational potential. We will refer to all models that do not include stochastic effects as collisionless. Stochasticity is an inevitable feature of real galaxies, arising from the gravitational influence of



Original content from this work may be used under the terms of the [Creative Commons Attribution 4.0 licence](https://creativecommons.org/licenses/by/4.0/). Any further distribution of this work must maintain attribution to the author(s) and the title of the work, journal citation and DOI.

passing stars and molecular clouds, transient spiral structure, dark matter substructure, accretion and infall from the circumgalactic environment, etc. (Pichon & Aubert 2006; Binney 2013) (to say nothing of the bar’s fluctuating pattern speed and strength, overlap of resonances from other non-axisymmetric structure, and so on—see Minchev et al. 2012; Wu et al. 2016; Fujii et al. 2018; Daniel et al. 2019). Stochasticity is also inherent to simulated galaxies, e.g., because of the necessity of representing the dynamics of a very large number N of stars/dark matter particles with a much smaller number of simulated particles, which always results in some level of numerical diffusion (Weinberg & Katz 2007a, 2007b; Sellwood & Debattista 2009; Ludlow et al. 2019, 2021; Wilkinson et al. 2023).

Regardless of the source of diffusion, the implicit justification for using collisionless theory in the past to describe resonant dynamics has been that the libration period of particles trapped in a resonance, despite being much longer than the orbital period t_{cross} , is still very short compared to the relaxation timescale t_{relax} . The latter quantity is defined as the timescale on which a particle’s action undergoes a relative change of order unity due to stochastic effects. For instance, in the case of two-body diffusion, $t_{\text{relax}} \sim N t_{\text{cross}}$. Yet for processes like bar–halo friction that depend sensitively on resonant features, the important diffusive timescale is not the relaxation time at all, but rather the time to diffuse across the width of the resonance $t_{\text{diff}} \ll t_{\text{relax}}$. When t_{diff} is comparable to or smaller than the libration period, conclusions drawn from collisionless theory may need to be revised.

The purpose of the present paper is to confront this “collisional” reality in the simplest possible model. To do this, we develop a reduced kinetic description for an ensemble of particles in the vicinity of a bar resonance, including stochastic kicks. In our kinetic equation, the secular part of the problem, namely the smooth particle–bar interaction, is treated using slow–fast angle–action variables and the pendulum approximation (Chirikov 1979; Monari et al. 2017), while the stochastic effects are assumed to impact only the slow actions and are lumped crudely into a single diffusion coefficient D (which we do not attempt to calculate self-consistently). This reduced problem then turns out to be mathematically identical to a problem previously studied in the theory of tokamak fusion plasma devices (Berk et al. 1997; Duarte et al. 2019; see also Pao 1988). In the tokamak context, stars are replaced with energetic ions, the galactic bar is replaced with a long-lived Alfvén wave, and the stochasticity stems not from molecular cloud passages or dark matter substructure but from collisions between the minority energetic ion species and the background thermal ion and electron species. Much like galactic dynamicists, tokamak theorists are interested in how the particle DF is heated on timescales much longer than the particles’ characteristic orbital period. What tokamaks and galaxies have in common is an underlying integrable mean-field structure that admits quasiperiodic orbits, and resonant wave–particle interactions that slowly modify those orbits. Several results can, therefore, be pulled from the tokamak literature that have not previously been employed in a stellar–dynamical context.

Perhaps the paradigmatic example of secular particle–bar interaction is the calculation of the dynamical friction torque on a bar embedded in a spherical dark matter halo (Hernquist & Weinberg 1992; Debattista & Sellwood 2000; Athanassoula 2003). In a classic example of collisionless theory, Tremaine & Weinberg (1984) analyzed this problem and found that, if one

artificially freezes the bar’s pattern speed, then in the time-asymptotic limit, the DF of resonantly trapped dark matter particles phase mixes completely, and the resulting symmetry leads to a vanishing torque on the bar (see also Chiba & Schönrich 2022). As an application of our theory, we revisit this problem here in a more general, collisional framework, and show that diffusion always injects some level of asymmetry into the DF, even in the time-asymptotic limit. This result carries implications for the evolution of bars in both real and simulated halos, the tension between which continues to challenge standard cosmological models (Roshan et al. 2021).

The rest of this paper is organized as follows. In Section 2, we recap the basic angle–action formalism required to describe the secular dynamics of a single test particle near resonance in a rigidly rotating potential. In Section 3, we consider an ensemble of such particles, and we write down and solve the kinetic equation that includes both this secular effect and a diffusive term. In Section 4, we apply what we have learned to the calculation of the dynamical friction felt by a galactic bar through coupling with its host dark matter halo. In Section 5, we comment on the limitations of our theory, discuss implications of our results for bar evolution in both real and simulated galaxies, and explain the relation of this work to existing literature in plasma physics. We summarize in Section 6.

2. Dynamics of a Test Particle near Resonance

In this section, we focus on the dynamical evolution of a test particle orbiting in a smooth galactic potential that includes a rigidly rotating bar perturbation, ignoring any stochastic effects. We show that, near a resonance, the motion of the particle through phase space can be effectively reduced to that of a pendulum. This is a classic calculation (Chirikov 1979) that has been employed numerous times in galactic dynamics (Tremaine & Weinberg 1984; Binney 2018; Sridhar 2019), but we repeat the key steps here in order to establish notation. We mostly follow the notational choices of Chiba & Schönrich (2022).

Let the gravitational potential of the galaxy be Φ . We suppose that Φ can be decomposed into a dominant, time-independent spherical background part Φ_0 , and a rigidly rotating bar perturbation $\delta\Phi$. Given the spherical symmetry of Φ_0 , it is natural to construct a spherical coordinate system $\mathbf{x} \equiv (r, \vartheta, \varphi)$ that is fixed in the inertial frame with origin at the center of the galaxy. We let the midplane of the galactic disk correspond to $\vartheta = \pi/2$, and let the bar be symmetric with respect to this midplane so that it rotates in the φ direction only with constant pattern speed Ω_p .

We have chosen Φ_0 to be spherical in order to facilitate comparison with the dynamical friction calculations of, e.g., Tremaine & Weinberg (1984), Banik & van den Bosch (2021), and Chiba & Schönrich (2022), where the test particles in question are dark matter particles and Φ_0 represents the dark matter halo potential, but it would be straightforward to modify our results to other contexts, such as to stars orbiting in the Galactic disk (Binney 2018), or stars trapped at orbital resonances in triaxial halo potentials (Yavetz et al. 2020). In practice, we will always take our background spherical potential to be a Hernquist sphere

$$\Phi_0 = -\frac{GM}{r_s + r}, \quad (1)$$

with total mass $M = 1.5 \times 10^{12} M_\odot$ and scale radius $r_s = 20$ kpc, and take the bar perturbation to be of the form

$$\delta\Phi(\mathbf{x}, t) = \Phi_b(r) \sin^2 \vartheta \cos[2(\varphi - \Omega_p t)], \quad (2)$$

$$\Phi_b(r) = -\frac{Av_c^2}{2} \left(\frac{r}{r_{\text{CR}}} \right)^2 \left(\frac{b+1}{b+r/r_{\text{CR}}} \right)^5, \quad (3)$$

where $r_{\text{CR}} = v_c/\Omega_p$ and $A = 0.02$, $b = 0.28$, $v_c = 238 \text{ km s}^{-1}$, and $\Omega_p = 35 \text{ km s}^{-1} \text{ kpc}^{-1} = 35.8 \text{ Gyr}^{-1}$. However, we will not need to use these explicit formulae until Section 4.4.

Now we consider an individual test particle orbiting in the combined potential Φ , and we aim to describe its dynamics in the inertial frame. Its Hamiltonian is

$$H = H_0 + \delta\Phi, \quad (4)$$

where

$$H_0 = \frac{v^2}{2} + \Phi_0(\mathbf{x}), \quad (5)$$

and \mathbf{v} is the particle's velocity in the inertial frame. The Hamiltonian H_0 is globally integrable, i.e., there exists a set of global angle-action coordinates $(\boldsymbol{\theta}, \mathbf{J})$ such that H_0 is a function of \mathbf{J} only. In practice, we take (Binney & Tremaine 2008)

$$\boldsymbol{\theta} = (\theta_r, \theta_\psi, \theta_\varphi), \quad \mathbf{J} = (J_r, L, L_z). \quad (6)$$

The angles $\boldsymbol{\theta}$ quantify the phase of oscillations in the radial direction, the phase of oscillations in the azimuthal direction within the particle's orbital plane, and the longitude of ascending node of the particle's orbit (which is fixed for spherical Φ_0), respectively. The corresponding actions \mathbf{J} quantify the amplitude of radial excursions, the total angular momentum, and the z -component of angular momentum of the particle's orbit. In the limit of a vanishingly weak bar perturbation $\delta\Phi \rightarrow 0$, the Hamiltonian $H = H_0$ only depends on \mathbf{J} ; in this case, the actions \mathbf{J} are perfectly conserved while the angles $\boldsymbol{\theta}$ evolve linearly as $\boldsymbol{\theta}(t) = \boldsymbol{\theta}(0) + \boldsymbol{\Omega}(\mathbf{J})t$, where

$$\boldsymbol{\Omega}(\mathbf{J}) \equiv \frac{\partial H_0}{\partial \mathbf{J}} = (\Omega_r, \Omega_\psi, \Omega_\varphi) \quad (7)$$

is the vector of orbital frequencies of the unperturbed problem. Because θ_φ is fixed for a particle orbiting a spherical potential, we always have $\Omega_\varphi = 0$.

Canonical Hamiltonian perturbation theory allows us to describe the modification of orbits by the finite bar perturbation $\delta\Phi$ (Binney & Tremaine 2008). However, canonical theory breaks down near orbital resonances, namely locations \mathbf{J}_{res} in action space such that

$$\mathbf{N} \cdot \boldsymbol{\Omega}(\mathbf{J}_{\text{res}}) = N_\varphi \Omega_p, \quad (8)$$

for some vector of integers $\mathbf{N} = (N_r, N_\psi, N_\varphi)$. To describe orbits in the vicinity of such resonances, it is best to make a canonical transformation to a new set of coordinates, which are again angle-action coordinates of the unperturbed problem (Lichtenberg & Lieberman 2013; Binney 2020a). Precisely, we map $(\boldsymbol{\theta}, \mathbf{J}) \rightarrow (\boldsymbol{\theta}', \mathbf{J}')$, where $\boldsymbol{\theta}' = (\theta'_f, \theta'_s)$ consists of the “fast” and “slow” angles⁴

$$\boldsymbol{\theta}'_f = (\theta_{f1}, \theta_{f2}) \equiv (\theta_r, \theta_\psi), \quad (9)$$

$$\theta'_s \equiv \mathbf{N} \cdot \boldsymbol{\theta} - N_\varphi \Omega_p t, \quad (10)$$

and $\mathbf{J}' = (\mathbf{J}_f, J_s)$ consists of the corresponding fast and slow actions

$$\mathbf{J}_f = (J_{f1}, J_{f2}) \equiv \left(J_r - \frac{N_r}{N_\varphi} L_z, L - \frac{N_\psi}{N_\varphi} L_z \right), \quad (11)$$

$$J_s \equiv L_z / N_\varphi. \quad (12)$$

Having made this transformation, we may rewrite H in terms of the new coordinates. It takes the form

$$H(\boldsymbol{\theta}', \mathbf{J}') = H_0(\mathbf{J}') - N_\varphi \Omega_p J_s + \sum_{\mathbf{k} \neq 0} \Psi_{\mathbf{k}}(\mathbf{J}') \exp(i\mathbf{k} \cdot \boldsymbol{\theta}'), \quad (13)$$

where $\mathbf{k} = (k_1, k_2, k_s)$ is a vector of integers and we have expanded $\delta\Phi$ as a Fourier series in the new angles $\boldsymbol{\theta}'$, i.e., written $\delta\Phi(\mathbf{x}, t) = \sum_{\mathbf{k}} \Psi_{\mathbf{k}}(\mathbf{J}') \exp(i\mathbf{k} \cdot \boldsymbol{\theta}')$. The coefficients $\Psi_{\mathbf{k}}$ are easily computed for the simple bar model (2)—see Tremaine & Weinberg (1984) and Appendix B of Chiba & Schönrich (2022). The special thing about the form (13) of the Hamiltonian is that it has no explicit time dependence (or rather, the time dependence has been absorbed into the definition of the angle θ'_s ; see Equation (10)).

The fast angles $\boldsymbol{\theta}'_f$ evolve on the orbital timescale, whereas θ'_s evolves on the much longer timescale $\sim (\mathbf{N} \cdot \boldsymbol{\Omega} - N_\varphi \Omega_p)^{-1}$. Thus, we may average H over the unimportant fast motion; the result is

$$\begin{aligned} \mathcal{H} &\equiv \frac{1}{(2\pi)^2} \int d\boldsymbol{\theta}'_f H(\boldsymbol{\theta}', \mathbf{J}') \\ &= H_0(J_s) - N_\varphi \Omega_p J_s + \sum_{\mathbf{k} \neq 0} \Psi_{\mathbf{k}}(J_s) \exp(ik\theta'_s), \end{aligned} \quad (14)$$

where we used the shorthand $\Psi_{(0,0,k)} = \Psi_k$, and the dependence on fast actions \mathbf{J}_f is now implicit. Hamilton's equations tell us that \mathbf{J}' evolves according to $d\mathbf{J}'/dt = -\partial\mathcal{H}/\partial\boldsymbol{\theta}' = (-\partial\mathcal{H}/\partial\theta'_s, 0, 0)$. Thus, the fast actions \mathbf{J}_f are constants under the time-averaged perturbation, and so at a fixed \mathbf{J}_f we find that the dynamics reduces to motion in the “slow plane” (θ'_s, J_s) . We can simplify \mathcal{H} further by exploiting the fact that we only care about motion in the vicinity of the resonance (indeed, we already made this restriction implicitly by assuming that θ'_s evolves much more slowly than $\boldsymbol{\theta}'_f$). To do this, let the resonant action \mathbf{J}_{res} from Equation (8) transform to $\mathbf{J}'_{\text{res}} = (\mathbf{J}_f, J_{s,\text{res}})$, define

$$I \equiv J_s - J_{s,\text{res}}, \quad \phi_k = \theta'_s + \frac{\arg \Psi_k}{k}, \quad (15)$$

and let $\phi_k \in (-\pi, \pi)$. Then Taylor expanding the right-hand side of (14) for small I and discarding constants and unimportant higher-order terms, we find⁵

$$\mathcal{H} \approx \frac{1}{2} H_0''(J_{s,\text{res}}) I^2 + 2 \sum_{k>0} |\Psi_k(J_{s,\text{res}})| \cos(k\phi_k). \quad (16)$$

Normally, it is the case that the sum over k in Equation (16) is dominated by a single, small value of k . Here, we will focus on resonances \mathbf{N} with $N_\varphi = 2$, because these give the dominant contributions to the dynamical friction on galactic bars, although

⁴ Formally, this mapping follows from the time-dependent generating function $s(\boldsymbol{\theta}, \mathbf{J}', t) = \theta_r J_{f1} + \theta_\psi J_{f2} + (\mathbf{N} \cdot \boldsymbol{\theta} - N_\varphi \Omega_p t) J_s$

⁵ For a discussion of the accuracy of the approximations made in deriving Equation (16), and the leading-order corrections to it, see Kaasalainen (1994), Binney (2018), and Binney (2020b).

the formalism we develop can be applied to other resonances with minimal adjustments. For $N_\varphi = 2$, the only contribution to Equation (16) is from $k = 1$ (Chiba & Schönrich 2022, Appendix B). The resulting simplified \mathcal{H} therefore takes the pendulum form (Chirikov 1979; Lichtenberg & Lieberman 2013):

$$\mathcal{H} = \frac{1}{2}GI^2 - F \cos \phi, \quad (17)$$

where $\phi \equiv \phi_1$ and

$$G \equiv \left. \frac{\partial^2 H_0}{\partial J_s^2} \right|_{J_{s,\text{res}}}, \quad F = -2|\Psi_1(J_{s,\text{res}})|. \quad (18)$$

In the cases of interest to us, $G < 0$, and of course, $F < 0$ always. An explicit expression for $-F$ is given in Equation (B9) of Chiba & Schönrich (2022).

The variables (ϕ, I) are canonical variables for the pendulum Hamiltonian (17). Their equations of motion are

$$\frac{d\phi}{dt} = \frac{\partial \mathcal{H}}{\partial I} = GI, \quad \frac{dI}{dt} = -\frac{\partial \mathcal{H}}{\partial \phi} = -F \sin \phi, \quad (19)$$

which are the equations of a simple pendulum. The pendulum moves at constant “energy” \mathcal{H} , either on an untrapped “circulating” orbit with $\mathcal{H} > F$ (so that ϕ periodically takes all values in $(-\pi, \pi)$) or on a trapped “librating” orbit with $\mathcal{H} < F$ (so that the pendulum oscillates around $(\phi, I) = (0, 0)$). The separatrix between the two orbit families has the equation $\mathcal{H} = F$. The period of infinitesimally small oscillations around $(\phi, I) = (0, 0)$ —the so-called libration time—is given by

$$t_{\text{lib}} \equiv \frac{2\pi}{\sqrt{FG}}. \quad (20)$$

The maximum width in I of the librating “island” is at $\phi = 0$, where it spans $I \in (-I_h, I_h)$ and I_h is the island half-width:

$$I_h \equiv 2\sqrt{\frac{F}{G}}. \quad (21)$$

Equations (20) and (21) are the fundamental scales involved in the dynamics of test particles governed by the pendulum Hamiltonian (17).

3. Kinetic Theory near a Resonance

In Section 2, we learned how to describe the dynamical evolution of a single resonant test particle in the smooth, rigidly rotating potential $\Phi_0 + \delta\Phi$. In this section, we will add a stochastic forcing to the dynamics. The motion of a single particle is no longer deterministic in this case, so we must turn to a statistical description of an ensemble of such test particles. We do this using a kinetic equation.

We wish to understand how an ensemble of particles behaves near a particular resonance N associated with the slow action $J_{s,\text{res}}$. Let us therefore consider particles that all share the same fast actions \mathbf{J}_f but may differ in their values of fast angles $\boldsymbol{\theta}_f$, slow angle θ_s , and slow action J_s . Averaging the ensemble over the fast angles, we can describe the resulting density of particles in the (ϕ, I) plane (Equation (15)) using a smooth distribution function (DF) that we call $f(\phi, I, t)$. The number of particles in the phase space area element $d\phi dI$ surrounding (ϕ, I) at time t is then proportional to $d\phi dI f(\phi, I, t)$. The kinetic equation

governing f is

$$\frac{\partial f}{\partial t} + \{f, \mathcal{H}\} = C[f], \quad (22)$$

where $\{\cdot, \cdot\}$ is a Poisson bracket encoding the smooth advection in the (ϕ, I) plane:

$$\{f, \mathcal{H}\} = \frac{\partial f}{\partial \phi} \frac{\partial \mathcal{H}}{\partial I} - \frac{\partial f}{\partial I} \frac{\partial \mathcal{H}}{\partial \phi}, \quad (23)$$

and $C[f]$ is a “collision operator” encoding the effect of stochastic fluctuations in the potential. For \mathcal{H} , we use the pendulum approximation (17), while for $C[f]$ we take a very simple diffusive form with constant diffusion coefficient D :

$$C[f] = D \frac{\partial^2 f}{\partial I^2}. \quad (24)$$

The diffusion coefficient D can be calculated from a given theoretical model of, e.g., scattering by passing stars and molecular clouds (Binney & Lacey 1988; Jenkins & Binney 1990; De Simone et al. 2004), dark matter substructure (Bar-Or et al. 2019; Peñarrubia 2019; El-Zant et al. 2020), or spurious numerical heating in simulations (Weinberg & Katz 2007a; Ludlow et al. 2021), and it can potentially be calibrated from data (Ting & Rix 2019; Frankel et al. 2020). The interested reader should refer to Section 3.1 for some quantitative estimates. We emphasize that we make no attempt at self-consistency here, as we simply impose a diffusion coefficient by hand, rather than calculating it from f . Similarly, we do not account at any stage for the self-gravity of the perturbed dark matter DF; in other words, the particles interact only with the bar, not with each other (Weinberg 1985; Dootson & Magorrian 2022).

Putting Equations (17) and (22)–(24) together, we have the kinetic equation:

$$\frac{\partial f}{\partial t} + GI \frac{\partial f}{\partial \phi} - F \sin \phi \frac{\partial f}{\partial I} = D \frac{\partial^2 f}{\partial I^2}. \quad (25)$$

In writing down Equation (25), we have made a few key assumptions:

1. We have ignored any diffusion in ϕ .
2. We have assumed that the diffusion coefficient D is a constant, independent of ϕ or I .
3. We have assumed that it is legitimate to consider an ensemble at fixed fast action \mathbf{J}_f , which implicitly ignores any diffusion in \mathbf{J}_f .

We can justify the first two assumptions heuristically on the grounds that the resonant island is narrow, i.e., the extent of the island in I is usually small compared to the whole of slow action space, whereas it spans the whole of slow angle (ϕ) space.⁶ As a result, the features in the DF created by the resonance are going to be much sharper in I than in ϕ , so a term like $\partial^2 f / \partial \phi^2$ in the collision operator is expected to be subdominant. Also, the narrowness of the island means we are only interested in the dynamics over a small portion of action space, so D ought not vary too much across the domain of interest and can be

⁶ This “narrow resonance approximation” is standard in tokamak plasma theory (Su & Oberman 1968; Callen 2014; Duarte et al. 2019; Tolman & Catto 2021).

estimated locally. The third assumption, namely that of no diffusion in \mathbf{J}_f , is difficult to justify in the general case; there is a priori no reason to assume that stochastic kicks in \mathbf{J}_f will be small compared to those in \mathbf{J}_s , and such kicks will couple different \mathbf{J}_f in a proper kinetic equation via terms like $\sim \partial^2 f / \partial J_f^2$. Nevertheless, we will stick with this assumption because it allows a great simplification of the kinetic theory, and the basic results and intuition we gain from solving the simplified theory will be invaluable when attacking more realistic problems. We discuss this assumption further in Section 5.

Before attempting to solve the kinetic Equation (25), one more simplification is in order. Naively, Equation (25) seems to depend on three parameters: G , F , and D . However, we can reduce this to one effective parameter by introducing certain dimensionless variables. First, we note that the typical timescale for a particle to diffuse all the way across the resonance (a distance $\sim 2I_h$ in action space) is the diffusion time,

$$t_{\text{diff}} \equiv \frac{(2I_h)^2}{2D} = \frac{8F}{GD}. \quad (26)$$

Now let us define the dimensionless variables:

$$\tau \equiv \sqrt{GF}t = \frac{2\pi t}{t_{\text{lib}}}, \quad (27)$$

$$j \equiv \sqrt{\frac{G}{F}}I = \frac{2I}{I_h}, \quad (28)$$

$$\Delta \equiv \sqrt{\frac{G}{F^3}}D = \frac{4 t_{\text{lib}}}{\pi t_{\text{diff}}}, \quad (29)$$

where the libration time t_{lib} is given in Equation (20) and the island half-width I_h is defined in Equation (21). Clearly, τ is a dimensionless measure of time normalized by the libration time, j is a dimensionless measure of the slow action variable relative to the resonant island width, and Δ is the diffusion strength, i.e., the ratio of the libration timescale to the diffusion timescale. Treating f as a function of these variables, i.e., writing $f(\phi, j, \tau)$, Equation (25) becomes

$$\frac{\partial f}{\partial \tau} + j \frac{\partial f}{\partial \phi} - \sin \phi \frac{\partial f}{\partial j} = \Delta \frac{\partial^2 f}{\partial j^2}. \quad (30)$$

We see that, in these variables, the kinetic equation depends on the single dimensionless parameter Δ , which we discuss next.

3.1. The Diffusion Strength Δ

The dimensionless diffusion strength $\Delta \approx t_{\text{lib}}/t_{\text{diff}}$ (Equation (29)) plays a central role in this work, because it measures the importance of diffusion relative to that of the bar perturbation near resonance. The regime $\Delta \gg 1$ corresponds to very strong diffusion, whereas $\Delta \ll 1$ corresponds to very weak diffusion; the “collisionless limit” favored by many classic calculations corresponds to $\Delta = 0$ (see Section 1). A key aim of this paper is to understand how the behavior of a DF near a resonance depends on Δ , and how this might affect galactic phenomena like bar-halo friction. As we will see, even for Δ values as small as ~ 0.1 , the behavior predicted by the kinetic

Equation (30) can be significantly different from the collisionless limit.

We can estimate Δ heuristically by noting that t_{diff} is related to the relaxation time t_{relax} , which is the time required for any stochastic process to change a particle’s action by order of itself (Binney & Tremaine 2008; Fouvry & Bar-Or 2018). If we assume the diffusion coefficient D is roughly constant over the whole of action space (which is a gross oversimplification but will suffice for an order-of-magnitude estimate), then from Equation (26) we have

$$\frac{t_{\text{diff}}}{t_{\text{relax}}} \sim \left(\frac{I_h}{J_{s, \text{res}}} \right)^2 \sim \left| \frac{\Psi_1}{H_0} \right| \sim A \ll 1. \quad (31)$$

Here, A is the dimensionless strength of the bar (Equation (3)); for the Milky Way, $A \sim 0.02$ (Chiba et al. 2020). Putting Equations (29) and (31) together, we estimate

$$\Delta \sim \frac{t_{\text{lib}}}{A t_{\text{relax}}} \quad (32)$$

$$\sim 10 \times \left(\frac{A}{0.02} \right)^{-1} \left(\frac{t_{\text{lib}}}{2 \text{ Gyr}} \right) \left(\frac{t_{\text{relax}}}{10 \text{ Gyr}} \right)^{-1}. \quad (33)$$

Typically, important Galactic bar resonances like the corotation resonance have libration times of $t_{\text{lib}} \sim 2$ Gyr (see Section 4 for examples). The relaxation time t_{relax} depends on the context in which the kinetic equation is being applied, because diffusion can be driven by a variety of different causes, including transient spiral arms, finite- N granularity noise, etc. But regardless of the context, we see immediately from the estimate (33) that Δ can be of order unity even for systems with relaxation times much longer than a Hubble time.

To be more quantitative, let us consider a virialized, isolated dark matter halo of enclosed mass $M(r)$ made up of particles of mass m and velocity dispersion $\sigma(r)$. Then the two-body relaxation time for the dark matter particles is (Binney & Tremaine 2008)

$$t_{\text{relax}} \sim \frac{\sigma^3 r^3}{G^2 m M} \sim N t_{\text{cross}}, \quad (34)$$

where $N = M/m$ is the number of particles inside radius r , and we used $\sigma^2 \sim GM/r$ and introduced the typical crossing time $t_{\text{cross}} \sim \sigma/R$. Moreover, a reasonable estimate for the libration time is $t_{\text{lib}} \sim A^{-1/2} t_{\text{cross}}$. Plugging these results into (32) gives

$$\Delta \sim \frac{1}{A^{3/2} N} \approx 0.1 \times \left(\frac{A}{0.01} \right)^{-1} \left(\frac{N}{10^4} \right)^{-1}, \quad (35)$$

where the quantities on the right-hand side should be evaluated at the location of the important resonances (usually $r \lesssim 10$ kpc). For standard cold dark matter models, N is enormous, which results in a negligible $\Delta \ll 1$, rendering collisionless theory valid. However, in numerical simulations of cold dark matter halos, N is the number of particles used to represent the halo inside the resonant radius, which is often comparable to 10^4 or 10^5 within 10 kpc (Ludlow et al. 2019, 2021). It follows that numerical noise alone can produce an effective $\Delta \sim 0.1$. Similarly, Δ may be non-negligible in alternative dark matter models; for instance, in fuzzy dark matter theory, particles with true masses $m \sim 10^{-22}$ eV behave collectively as quasiparticles of size ~ 1 kpc and effective mass $m_{\text{eff}} \gtrsim 10^7 M_\odot$ (see Equation

⁷ We note that f still depends parametrically on N and \mathbf{J}_f , though we are suppressing the explicit dependence here to keep the notation clean.

(38) of Hui et al. 2017), so a halo of enclosed mass $M = 10^{11} M_\odot$ would behave as if it were constituted of $N \sim 10^4$ particles, again giving $\Delta \sim 0.1$.

As another example, we might let our DF f describe not dark matter particles but instead stars trapped near bar resonances in the Milky Way disk (Monari et al. 2017; Trick et al. 2019; Dootson & Magorrian 2022). In this case, one can set t_{relax} equal to the typical diffusion timescale for the orbital actions of disk stars, as measured from kinematic and chemical data from GAIA and APOGEE (i.e., the “age–velocity dispersion relation”; see Mackereth et al. 2019; Frankel et al. 2020). These measurements suggest that t_{relax} is on the order of the age of the galaxy; it follows from Equation (32) that typical Δ values are $\gtrsim 1$. Of course, such estimates ignore the fact that the bar resonances themselves likely have some influence on the diffusion of stars, in particular when they overlap with other bar resonances and/or resonances associated with spiral waves (Minchev & Famaey 2010), meaning it may be unrealistic to decouple secular and stochastic effects like we have proposed here. We assume throughout this paper that resonances are isolated, so we can make no quantitative statement here about the effect of resonance overlap. We leave this as an avenue for careful future study.

3.2. Solving the Kinetic Equation

Unfortunately, the kinetic Equation (30) cannot be solved analytically in general. In this section, we present time-dependent numerical solutions to (30) for a simple choice of initial DF and for various values of Δ . In particular, we find that the solution always tends toward some steady-state form. There are two interesting classes into which the steady-state solutions fall—for $\Delta \ll 1$, the steady DF is dominated by the resonant island structure, while for $\Delta \gg 1$, it is dominated by diffusion and the resonance leaves little trace. In fact, these limiting cases have already been investigated analytically in the context of wave–particle interactions in plasma (Pao 1988; Berk & Breizman 1998; Duarte et al. 2019). Inspired by these works, in Appendix A.1 and Appendix A.2, we derive some analytical solutions to (30) in the $\Delta \ll 1$ and $\Delta \gg 1$ limits, respectively. We will refer to those solutions throughout this section in order to illuminate our numerical results.

Let the initial global distribution of particles be a function of unperturbed actions \mathbf{J} only, so by Jeans’ theorem the initial “background” DF $f_0(\mathbf{J})$, normalized such that $\int d\theta d\mathbf{J} f_0 = 1$, is a steady-state solution of the unperturbed collisionless Boltzmann equation governed by $H_0(\mathbf{J})$ (Binney & Tremaine 2008). Because the canonical transformation $(\theta, \mathbf{J}) \rightarrow (\theta', \mathbf{J}')$ does not mix up angles and actions (Equations (10)–(11)), it follows that, when written in the new coordinates, f_0 will just be a function of \mathbf{J}' . In the language of the dimensionless variables we used to write down Equation (30), at fixed \mathbf{J}_f the initial DF in the (ϕ, j) plane will depend only on j , so $f_0 = f_0(j)$.

For simplicity, we will only focus on DFs that are initially linear in j . This is well motivated, provided the resonance is narrow (Section 3), because any initial DF that depends only on j can be Taylor expanded around the resonance at $j = 0$ to give a locally linear form. Thus, we take as our initial condition

$$f(\phi, j, \tau = 0) = f_0(j = 0) + \alpha j \equiv f_{\text{init}}(j), \quad (36)$$

where

$$\alpha \equiv \left. \frac{\partial f_0}{\partial j} \right|_{j=0}. \quad (37)$$

Of course, the linear approximation (36) should be corrected in detailed modeling (Pao 1988), but it is sufficient to elucidate the main physics of Equation (30) (White & Duarte 2019).

At $t = 0$, we switch on the bar potential, and the resulting evolution is described by Equation (30). Of course, this is not realistic—true galactic bars do not just appear out of nowhere, but instead they grow gradually in strength in the first few Gyr of the galaxy’s lifetime. However, the qualitative results one finds by growing the bar slowly are not too different from imposing it instantaneously at $t = 0$ (Chiba & Schönrich 2022).⁸ For simplicity, we will consider only an instantaneously emerging bar here, but time-dependent bar strengths (and pattern speeds) will be considered in future work.

3.2.1. Numerical Method

We solve Equation (30) numerically on a regular grid in (ϕ, j) space, with 200 cells in ϕ (from $\phi_{\text{min}} = -\pi$ to $\phi_{\text{max}} = \pi$) and 4000 cells in j (from $j_{\text{min}} = -20\pi$ to $j_{\text{max}} = 20\pi$). For the integration, we use an explicit forward-Euler scheme, which is first-order accurate in τ and second-order accurate in ϕ and j . We also set $f(\phi, j_{\text{min,max}}, \tau) = f_{\text{init}}(\phi, j_{\text{min,max}})$ in order to satisfy the boundary condition that $f \rightarrow f_{\text{init}}$ for very large $|j|$ (see Section 3.3.3). Because we are solving on a grid, we inevitably have some numerical diffusion, which makes it hard to resolve the smallest-scale structures that arise at late times for very small Δ ; to avoid this issue, we report numerical results only for $\Delta \geq 0.001$. The case $\Delta = 0$ can be solved analytically (Chiba & Schönrich 2022).

3.3. Results

We can most easily examine the nature of the resulting solutions by defining a dimensionless auxiliary DF:

$$g(\phi, j, \tau) \equiv \frac{f(\phi, j, \tau) - f_0(0)}{\alpha}, \quad (38)$$

which measures the modification of f compared to its background value on resonance $f_0(0)$; it is obvious from (36) that $g(\phi, j, \tau = 0) \equiv g_{\text{init}}(j) = j$. Figure 1 shows colored contours of this initial distribution, overlaid by black contours of the Hamiltonian \mathcal{H} (Equation (17)). The separatrix between librating and circulating orbit families is shown with a dashed black line.

In Figure 2, we plot contours of the numerical solution $g(\phi, j, \tau)$ for $\Delta = 0.001, 0.1, 1, 10$ in rows (a)–(d), respectively. In each row, from left to right, we plot the solution at different “times” $\Delta^{1/3} \tau$.

First, we consider row (a), which is in the limit of very weak diffusion ($\Delta = 0.001$). Physically, we expect that, in this limit, the DF will phase mix around and within the resonant island. The reason for phase mixing is that, in the absence of diffusion ($\Delta = 0$), the trajectories of individual particles trace contours of

⁸ In fact, Chiba & Schönrich (2022) show that, in the collisionless regime, the DF exhibits sharper features near the separatrix when the bar is grown slowly than when it is imposed instantaneously. Because diffusion feeds off sharp features in the DF (Equation (24)), diffusive effects may be even more important in this case.

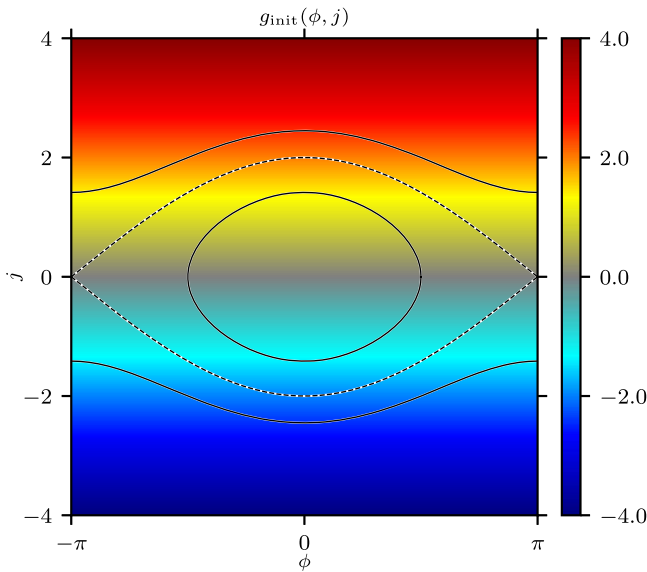


Figure 1. Colors show contours of the initial condition $g_{\text{init}}(\phi, j) \equiv g(\phi, j, 0) = j$, where g is related to the DF f through Equation (38). We overlay with solid black lines contours of the pendulum Hamiltonian \mathcal{H} . The separatrix between librating and circulating regions is shown with a black dashed line.

constant \mathcal{H} in the (ϕ, j) plane; and because adjacent contours correspond to slightly different libration/circulation periods, the initial DF gets sheared out along these contours, producing ever finer-scale structures in the phase space. If Δ were exactly zero, and in the absence of any coarse graining, this process would continue indefinitely. However, for our very small but finite value of $\Delta = 0.001$, diffusion is able to wipe out the finest-grained features without needing to invoke any coarse graining.⁹ We see that, by the third column, $g \approx 0$ inside the separatrix, and it is smeared almost evenly on contours of constant \mathcal{H} outside of the separatrix. The DF has reached steady state.

Now let us consider row (d), which corresponds to the opposite limit of very strong diffusion, represented here by $\Delta = 10$. In this case, the resonance has little effect on g at any time. This again is as expected, because the initial linear DF (36) is annihilated by the collision operator $C[f]$ (Equation (24)). In other words, wherever the bar perturbation induces some curvature in the DF, strong diffusion immediately acts to remove it and restore the linear initial condition.

The cases $\Delta = 0.1$ and $\Delta = 1$ (rows (b) and (c)) are intermediate between these two extremes. In the following subsections, we further unpack the different features of these solutions and explain how their behavior depends on Δ . A reader who is satisfied with the basic picture shown in Figure 2 can skip these details and go directly to the more astrophysically interesting Section 4.

3.3.1. Skew Symmetry

In every panel of Figure 2, we notice the following skew-symmetry property:

$$g(\phi, j, \tau) = -g(-\phi, -j, \tau). \quad (39)$$

⁹ In reality, all systems have a finite number of particles, and hence a nonzero Δ , regardless of how much one tries to suppress diffusion; there is no such thing as a perfectly collisionless system (Beraldo e Silva et al. 2019).

This follows easily from the symmetry of Equation (30) under the replacements $\phi \rightarrow -\phi$ and $j \rightarrow -j$, and the corresponding antisymmetry of the initial condition $g_{\text{init}}(j) = j$.

3.3.2. Steady State

In each row (a)–(d) of Figure 2, we find that, by the third column, the solution has approximately reached its steady state, which reach reflects a balance between the secular bar torque (which wants to churn the DF around the island) and diffusion (which wants to restore the linear initial condition). The fact that a steady state is possible when our externally imposed diffusion is constantly injecting energy into the system is a consequence of (i) the fact that the boundary condition is set to match the unperturbed DF at $\pm \infty$, which acts as a particle source/sink.

How long does it take to reach the steady state? For $\Delta \ll 1$, where the bar resonance dominates, the typical steady-state timescale is a few libration periods, say

$$t_{\text{steady}} \sim 3 t_{\text{lib}} \sim 3 \Delta t_{\text{diff}}, \quad (\Delta \ll 1), \quad (40)$$

which corresponds to $\Delta^{1/3} \tau_{\text{steady}} \lesssim 20$ —see Equation (27). Thus, in this weakly diffusive limit, we typically have $t_{\text{lib}} \ll t_{\text{steady}} \ll t_{\text{diff}}$. Meanwhile in the diffusion-dominated regime $\Delta \gg 1$, we show in Appendix A.2 that

$$t_{\text{steady}} \sim \frac{t_{\text{lib}}}{\Delta^{1/3}} \sim \Delta^{2/3} t_{\text{diff}}, \quad (\Delta \gg 1) \quad (41)$$

i.e., $\Delta^{1/3} \tau_{\text{steady}} \sim 2$. Hence, in this case, we have the hierarchy $t_{\text{diff}} \ll t_{\text{steady}} \ll t_{\text{lib}}$. In general, for a given bar strength, stronger diffusion always leads to a more rapidly achieved steady state.

3.3.3. Angle-averaged Distribution

It is instructive to average the solution $f(\phi, j, \tau)$ over the slow angle ϕ and investigate the resulting DF

$$\langle f \rangle_\phi \equiv \frac{1}{2\pi} \int_{-\pi}^{\pi} d\phi f(\phi, j, \tau). \quad (42)$$

In Figure 3, we plot the corresponding auxiliary DF (see Equation (38)),

$$\langle g - g_{\text{init}} \rangle_\phi = \frac{\langle f \rangle_\phi - f_0(0)}{\alpha} - j, \quad (43)$$

as a function of j for the same Δ values as in Figure 2. In panels (a)–(c), we show this quantity for times $t/t_{\text{lib}} = 0.25, 1$, and 40 , respectively; in particular, we know from Section 3.3.2 that panel (c) always corresponds to the steady state. The vertical dotted lines in these panels are at $j = \pm 2$, which marks the maximum extent of the separatrix in the (ϕ, j) plane (Figures 1, 2). We notice immediately that $\langle g - g_{\text{init}} \rangle_\phi$ is an odd function of j , which follows from the skew symmetry (39), and that in the steady-state (panel (c)) it exhibits a single maximum and a single minimum. For very small Δ , the amplitude of these extrema actually grows with Δ , peaking around $\Delta \sim 0.01$, before decaying as Δ is increased further. Furthermore, in the very small Δ limit, the location of the extrema is $|j| \approx 1.5$, which is inside the maximum extent of the separatrix. Increasing Δ broadens the distribution and shifts the locations of the extrema to larger $|j|$. For instance, for $\Delta = 1$, the amplitude of the $\langle g - g_{\text{init}} \rangle_\phi$ curve is around half of what it was for $\Delta = 0.001$, while the locations of its extrema have shifted outside the separatrix to $|j| \approx 2.5$. In the strong-diffusion

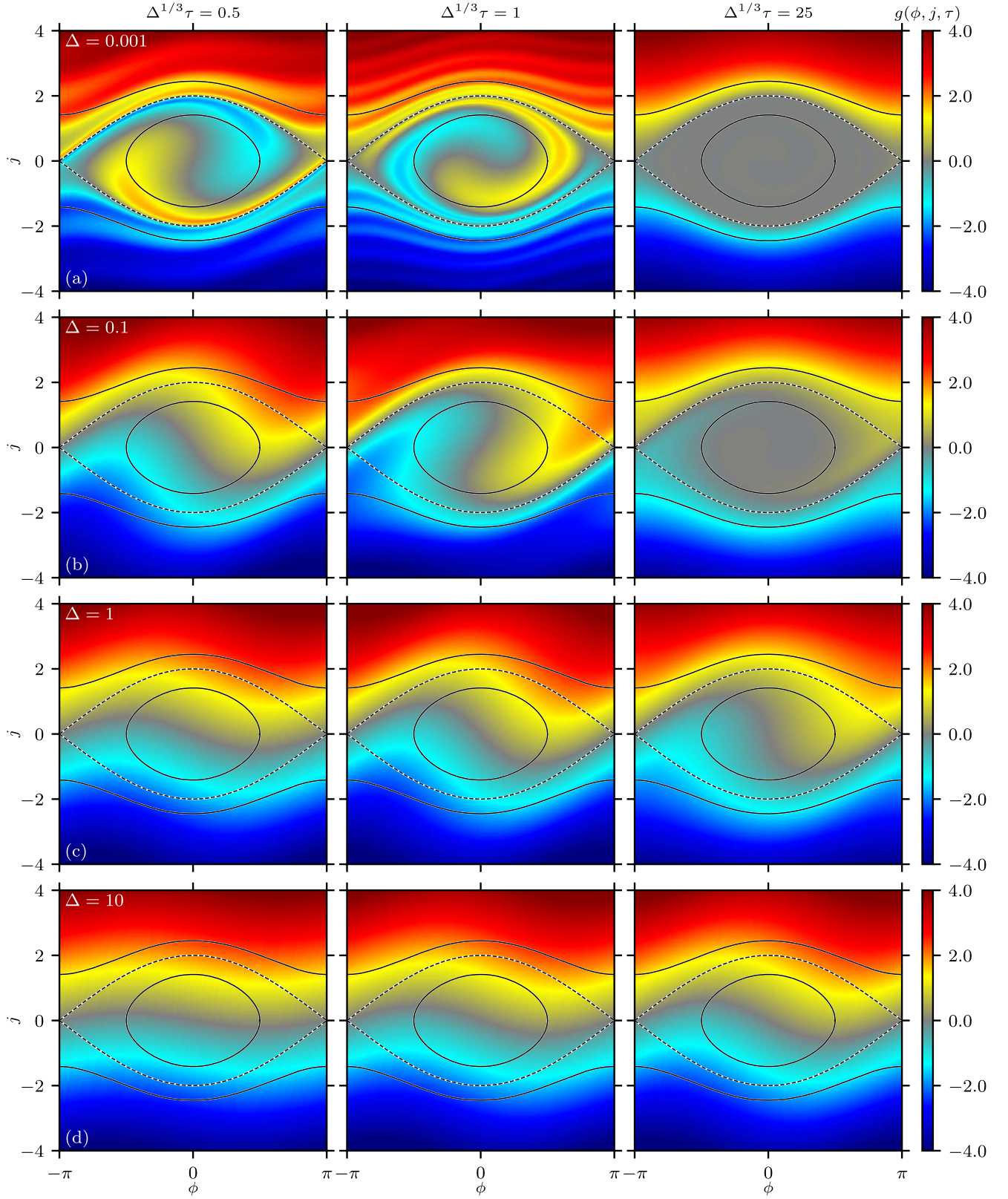


Figure 2. Contours of $g(\phi, j, \tau)$ (related to f through Equation (38)), computed by solving the kinetic Equation (30) numerically with the initial condition shown in Figure 1. In rows (a)–(d), we show the time evolution of the solution for $\Delta = 0.001, 0.1, 1$, and 10 , respectively. The right column represents the steady-state solution.

regime $\Delta \gg 1$, the distribution becomes very broad and its amplitude decreases dramatically.

We note that $\langle g - g_{\text{init}} \rangle_\phi$ does not appear to decay toward zero at large $|j|$. This is a well-known artifact of choosing the background DF to be linear and the collision operator to be of

diffusion form (Duarte & Gorelenkov 2019); if we chose a Krook operator instead, we would not have the same issue. This is the reason we force a boundary condition at the edge of the grid in j (see Section 3.2.1). We take the grid in j to be sufficiently large that the sharp boundary does not feed back on

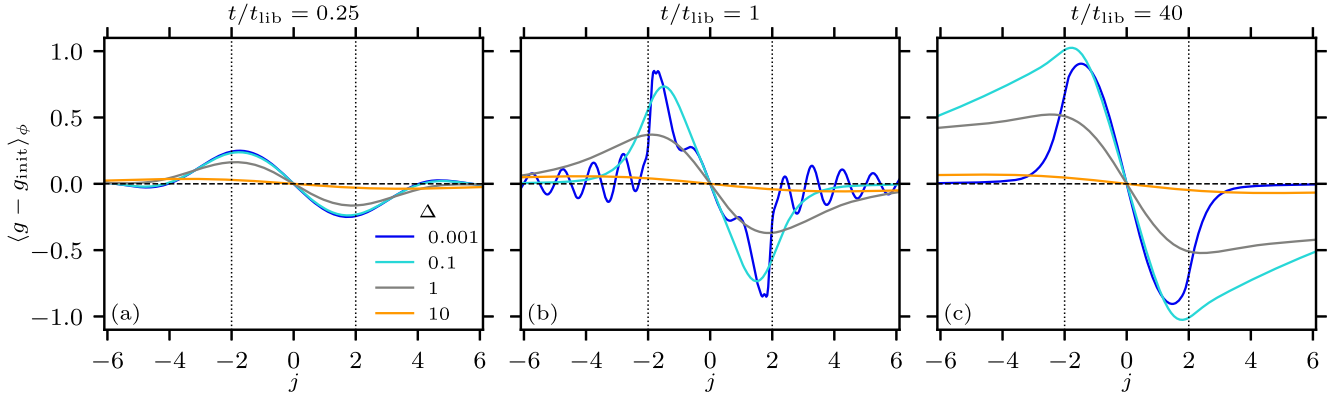


Figure 3. Time evolution of the slow-angle-averaged perturbation to the DF, $\langle g - g_{\text{init}} \rangle_\phi$ (see Equation (43)), for the same values of Δ as used in Figure 2. The right-hand panel represents the steady-state solution. The vertical dotted lines show the maximum extent of the separatrix, $j = \pm 2$.

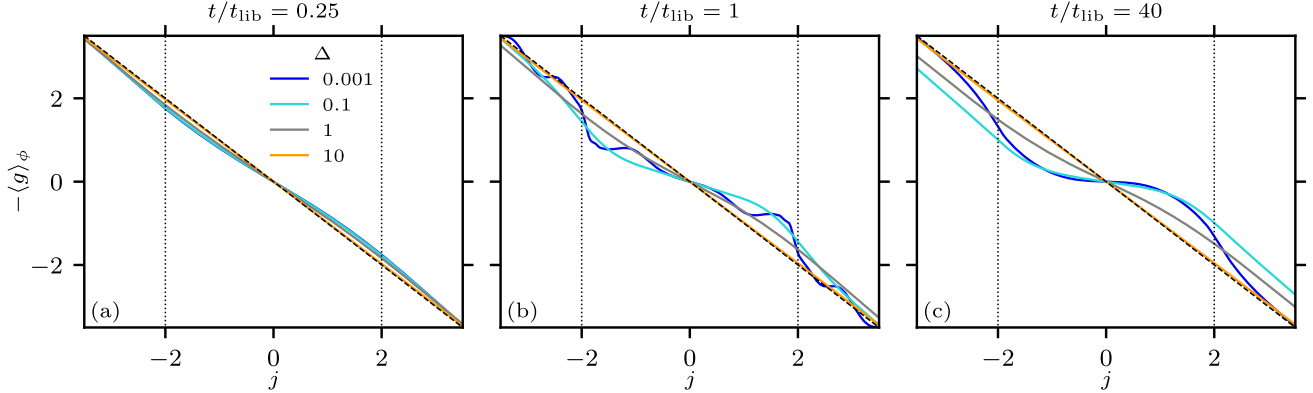


Figure 4. As in Figure 3, except we show the evolution of $-\langle g \rangle_\phi$, which is the dimensionless representation of a linearly decreasing angle-averaged DF.

the near-resonant dynamics. This issue also does not affect the bar-halo friction calculations in Section 4, because these are sensitive only to the angle-dependent part of the DF, which does decay for large $|j|$.

To make clearer the evolution of the angle-averaged DF, we present Figure 4, in which we use the same data as in Figure 3 but this time we simply plot $-\langle g \rangle_\phi$. This is a dimensionless representation of an initially linearly decreasing, angle-averaged DF. We see that, for very small $\Delta \ll 1$ and late times (panel (c), blue lines), the angle-averaged DF has flattened in the vicinity of the resonance. Increasing Δ broadens the resonance, allowing it to affect larger j values, but also weakens it, so that for very large $\Delta \gg 1$ (orange lines) the DF barely evolves at all. We will quantify the broadening and weakening in Figure 5 below (see Section 3.3.4).

In Figure 6(a), we plot the maximum value of $\langle g - g_{\text{init}} \rangle_\phi$ in steady state as a function of Δ . We see that this quantity is roughly constant at small $\Delta \ll 1$, and of order unity in amplitude. For large $\Delta \gg 1$, it decays like $\propto \Delta^{-1}$, which can also be shown analytically (Duarte et al. 2019, Equation (13)). It makes physical sense that the maximum value of $\langle g - g_{\text{init}} \rangle_\phi \rightarrow 0$ as $\Delta \rightarrow \infty$, because for infinitely strong diffusion the DF should never evolve from its linear initial condition.

3.3.4. Asymmetry in Slow Angle

Finally, when computing the dynamical friction torque on the bar in Section 4, it will turn out that the key quantity we must extract from our kinetic theory is $\text{Im } f_1(j, \tau)$, where f_1 is the first

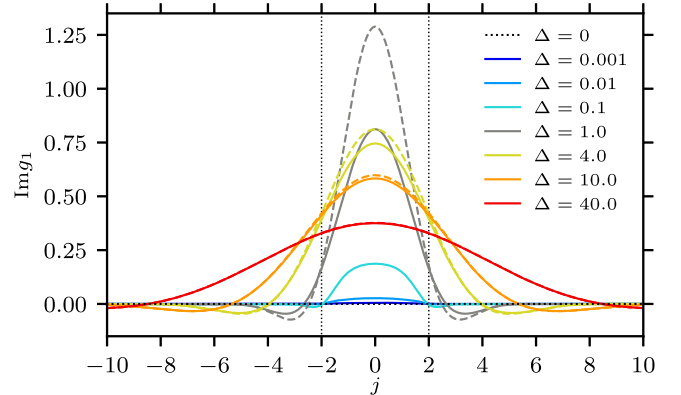


Figure 5. Plot of $\text{Im } g_1(j, \tau) \equiv \alpha^{-1} \text{Im } f_1(j, \tau)$ —see Equation (44)—as a function of j in the steady state for $\tau \rightarrow \infty$. Solid lines show the “exact” result from the numerical solution of Equation (30). Dashed lines show the analytical prediction from Equations (46)–(47) for $\Delta \geq 1$. The vertical dotted lines again show the maximum extent of the separatrix, $j = \pm 2$.

Fourier coefficient of the DF:

$$f_1(j, \tau) \equiv \frac{1}{2\pi} \int_{-\pi}^{\pi} d\phi f(\phi, j, \tau) \exp(-i\phi). \quad (44)$$

This quantity is obviously a measure of the asymmetry of the (slow) angular distribution of particles; when there is no such asymmetry, there can be no frictional torque.

In Figure 5, we plot the dimensionless quantity $\text{Im } g_1 = \alpha^{-1} \text{Im } f_1$ as a function of j in the steady state $\tau \rightarrow \infty$, for various Δ . We see from Figure 5 that $\text{Im } g_1$ is always even in

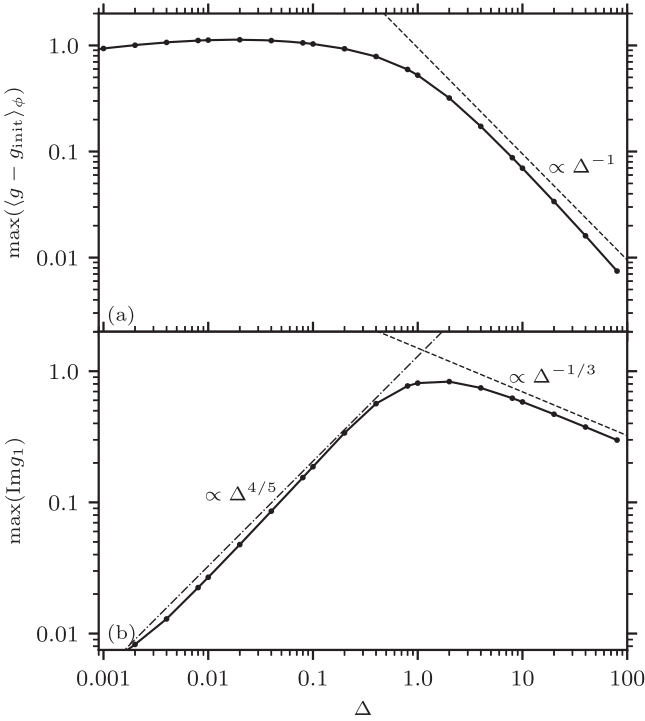


Figure 6. Plots of the maximum steady-state values of (a) $\langle g - g_{\text{init}} \rangle_\phi$ (see Figure 3) and (b) $\text{Im } g_1$ (see Figure 5) as functions of Δ .

j , which follows from the skew symmetry (39). Its amplitude is very small in the weak-diffusion regime $\Delta \ll 1$, reflecting the (approximate) symmetry in ϕ of the (nearly) phase-mixed steady-state—see Figures 2(a) and (b). Indeed, we know that, in the perfectly collisionless regime,

$$\text{Im } g_1(j, \tau \rightarrow \infty) = 0, \quad (\Delta = 0) \quad (45)$$

However, once the diffusion strength Δ is increased beyond ~ 0.1 , the peak value of $\text{Im } g_1$ grows significantly, then begins to decay with Δ for $\Delta \gg 1$. The dashed curves we show for $\Delta \geq 1$ in this plot correspond to the approximate analytic solution valid for $\Delta \gg 1$ derived in Appendix A.2, namely

$$\text{Im } g_1(j, \tau \rightarrow \infty) \approx \frac{\pi}{2} \mathcal{R}_\Delta(j), \quad (\Delta \gg 1), \quad (46)$$

where

$$\mathcal{R}_\Delta(j) \equiv \frac{1}{\pi \Delta^{1/3}} \int_0^\infty dy \exp\left(-\frac{y^3}{3}\right) \cos\left(\frac{jy}{\Delta^{1/3}}\right). \quad (47)$$

It is not hard to show that $\mathcal{R}(j)$ has the properties of a collisionally broadened resonance function (Duarte et al. 2019), namely $\int_{-\infty}^\infty dj \mathcal{R}_\Delta(j) = 1$ and $\lim_{\Delta \rightarrow 0} \mathcal{R}_\Delta(j) = \delta(j)$. We see from Figure 5 that the approximation (46) is accurate to within several percent or better for $\Delta \gtrsim 4$. It is also apparent from Figure 5 that the width of the $\text{Im } g_1(j, \tau \rightarrow \infty)$ curve increases monotonically with Δ . Indeed, in the $\Delta \gg 1$ limit, we know from Equations (46)–(47) that this width grows like $\propto \Delta^{1/3}$, and that the total area under the $\text{Im } g_1(j, \tau \rightarrow \infty)$ curve is constant.

The reason for this lack of Δ dependence at large $\Delta \gg 1$ is that strong diffusion essentially renders the bar–halo interaction linear (see the discussion in Section 5). Unlike in the nonlinear phase, the linear dynamics is insensitive to time delay effects

that arise from successive integrations of the kinetic equation within a perturbative approach (Berk et al. 1996).

Last, in Figure 6(b) we extract the steady-state value of $\max(\text{Im } g_1)$ and plot it as a function of Δ . For small $\Delta \ll 1$, we have roughly $\max(\text{Im } g_1) \propto \Delta^{4/5}$. This is an empirical scaling that is hard to explain mathematically (see Appendix A.1). Intuitively, it stems from the fact that weak diffusion “fills in” the DF near the inner edge of the separatrix, where we would have $g = 0$ were there no diffusion at all. The amplitude of g in the filled-in “strip” is $\mathcal{O}(1)$, while the strip’s thickness grows monotonically with Δ . For large $\Delta \gg 1$, we see that $\max(\text{Im } g_1) \propto \Delta^{-1/3}$, which agrees with Equations (46) and (47). The transition between these two regimes occurs around $\Delta \sim 2$, where $\max(\text{Im } g_1) \sim 1$.

4. Bar–Dark Matter Halo Dynamical Friction

As a galactic bar ages, it transfers angular momentum to its host dark matter halo, and consequently its rotation rate slows. The mechanism responsible is dynamical friction: the bar produces a perturbation in the dark matter distribution function f and hence in the dark matter density, which then backreacts to produce a torque \mathcal{T} on the bar, draining its angular momentum. Problems of bar–halo coupling—and more generally the problem of angular momentum transfer between a massive perturber and a distribution of particles—have been the focus of many classic studies in galactic dynamics (e.g., Lynden-Bell & Kalnajs 1972; Tremaine & Weinberg 1984; Weinberg 1985; Debattista & Sellwood 1998; Athanassoula 2003) and continue to inspire modern research (Kaur & Sridhar 2018; Chiba et al. 2020; Banik & van den Bosch 2021; Collier & Madigan 2021; Lieb et al. 2021; Chiba & Schönrich 2022; Dootson & Magorrian 2022; Kaur & Stone 2022). They are also strongly analogous to wave–particle interaction problems in plasma (see the discussion in Section 5).

One can write down a rather general formula for the dynamical friction torque \mathcal{T} on the bar as follows. As we have throughout this paper, let the host dark matter halo be spherical and let the bar rotate around the z -axis and have potential $\delta\Phi(\mathbf{x}, t)$. From Hamilton’s equation, the z -component of the specific torque felt by an individual dark matter particle due to the bar is

$$\frac{dL_z}{dt} = -\frac{\partial \delta\Phi}{\partial \theta_\phi}. \quad (48)$$

Let the DF of dark matter particles be f , normalized such that $\int d\theta d\mathbf{J} f = 1$. Then by Newton’s third law and using $d\mathbf{x} d\mathbf{v} = d\theta d\mathbf{J}$, the total torque on the bar (divided by the mass of the halo) due to the dark matter particles is equal to

$$\mathcal{T}(t) = \int d\theta d\mathbf{J} f(\theta, \mathbf{J}, t) \frac{\partial \delta\Phi(\theta, \mathbf{J}, t)}{\partial \theta_\phi}. \quad (49)$$

The challenge is to compute f for a given perturbation $\delta\Phi$, and then perform the integral (49).

4.1. Linear Theory

Lynden-Bell & Kalnajs (1972, hereafter **LBK**) and Weinberg (2004) compute f using the linearized collisionless Boltzmann (Vlasov) equation, ignoring the self-gravity of the perturbation to the dark matter distribution. Fourier expanding the potential as $\delta\Phi = \sum_N \delta\Phi_N(\mathbf{J}, t) \exp(i\mathbf{N} \cdot \boldsymbol{\theta})$ and similarly for the DF f ,

the linear phase space response induced by the bar is

$$f_N(\mathbf{J}, t) = iN \cdot \frac{\partial f_0}{\partial \mathbf{J}} \int_0^t dt' \delta\Phi_N(\mathbf{J}, t') e^{-iN \cdot \Omega(t-t')}, \quad (50)$$

where $f_0(\mathbf{J})$ is the unperturbed DF. Then putting $\delta\Phi_N(\mathbf{J}, t) = \delta\Phi_N(\mathbf{J}) \exp(-iN_\varphi \Omega_p t)$ and performing the integral over t' , one finds a “linear torque” $\mathcal{T}_N^{\text{lin}} = \sum_N \mathcal{T}_N^{\text{lin}}$, where the contribution from resonance N is

$$\begin{aligned} \mathcal{T}_N^{\text{lin}}(t) &\equiv (2\pi)^3 N_\varphi \int d\mathbf{J} |\delta\Phi_N|^2 N \cdot \frac{\partial f_0}{\partial \mathbf{J}} \\ &\times \frac{\sin[(N \cdot \Omega - N_\varphi \Omega_p)t]}{N \cdot \Omega - N_\varphi \Omega_p}. \end{aligned} \quad (51)$$

Taking the time-asymptotic limit $t \rightarrow \infty$, one arrives at the classic “LBK torque formula”:

$$\begin{aligned} \mathcal{T}_N^{\text{LBK}} &\equiv (2\pi)^3 N_\varphi \int d\mathbf{J} |\delta\Phi_N|^2 N \cdot \frac{\partial f_0}{\partial \mathbf{J}} \\ &\times \pi \delta(N \cdot \Omega - N_\varphi \Omega_p), \end{aligned} \quad (52)$$

which predicts that angular momentum is transferred to and from the dark matter halo exclusively at resonances. Importantly, for many realistic dark matter DFs $f_0(\mathbf{J})$, the LBK torque is finite and negative, implying a long-term transfer of angular momentum away from the bar and hence a decay in its pattern speed. In practice, the time-asymptotic limit may not be valid, because the torque takes some time to converge, by which time the pattern speed may have changed significantly (Weinberg 2004). Nevertheless, the LBK formula (52) is a good benchmark against which we can compare the magnitude of the torque arising from more sophisticated calculations.

4.2. Nonlinear Theory

Because they employ linear theory, LBK and Weinberg (2004) do not account for the inevitable nonlinear particle trapping that occurs sufficiently close to each resonance. Recognizing this shortcoming, Tremaine & Weinberg (1984)—hereafter TW84—and Chiba & Schönrich (2022) include the particle trapping effect. To do this, they first convert to slow–fast angle-action variables (θ', \mathbf{J}') around each resonance N as in Section 2. In these variables, the total “nonlinear torque” on the bar \mathcal{T}^{nl} can be written as a sum over N of contributions

$$\mathcal{T}_N^{\text{nl}}(t) = \int d\theta' d\mathbf{J}' f(\theta', \mathbf{J}', t) N_\varphi \frac{\partial \delta\Phi(\theta', \mathbf{J}')}{\partial \theta_s}. \quad (53)$$

If we now Fourier expand the potential $\delta\Phi$ in slow angle space as in Equation (13), and also expand the DF as $f = \sum_k f_k(\mathbf{J}', t) \exp(ik \cdot \theta')$, then (53) reads

$$\mathcal{T}_N^{\text{nl}}(t) = -i(2\pi)^3 N_\varphi \sum_k k_s \int d\mathbf{J}' f_k(\mathbf{J}', t) \Psi_k^*(\mathbf{J}'), \quad (54)$$

where one must be careful to properly divide phase space into nonoverlapping subvolumes that are dominated by individual resonances (see Section 4.5 of Chiba & Schönrich 2022 for a discussion). Because we always choose our initial f to be independent of angles (i.e., dependent only on \mathbf{J}'), we know from Section 2 that there will be no fast-angle dependence in f at

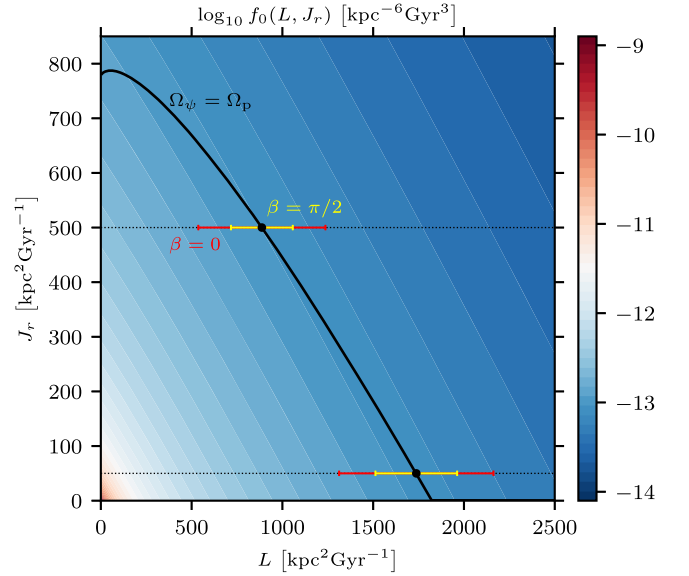


Figure 7. Contours of the isotropic Hernquist DF, $\log_{10}[f_0/(\text{kpc}^{-6} \text{Gyr}^3)]$, as a function of angular momentum L and radial action J_r for arbitrary inclination β . The solid black line shows the corotation resonance, $\Omega_\psi = \Omega_p = 35 \text{ km s}^{-1} \text{ kpc}^{-1}$, which is also independent of β . We choose two particular locations on the resonant line, shown with black dots, corresponding to $J_r = (500, 50) \text{ kpc}^2 \text{ Gyr}^{-1}$. Around each black dot, we show with red (yellow) “error bars” the maximum extent of the separatrix in L for $\beta = 0$ ($\beta = \pi/2$); these bars therefore mark out the region $j \in (-2, 2)$.

later times. This means that $f_k = \delta_{k_1}^0 \delta_{k_2}^0 f_{(0,0,k_s)}$, so

$$\mathcal{T}_N^{\text{nl}}(t) = 2(2\pi)^3 N_\varphi \sum_{k>0} k \int d\mathbf{J}' \text{Im}[f_k(\mathbf{J}', t) \Psi_k^*(\mathbf{J}')], \quad (55)$$

where we have used the shorthand $f_{(0,0,k)} = f_k$, and similarly for Ψ_k . At this stage, Chiba & Schönrich (2022) calculate the torque $\mathcal{T}_N^{\text{nl}}(t)$ by substituting for f_k the collisionless DF, i.e., the solution to the kinetic Equation (30) with $\Delta = 0$. In the time-asymptotic limit they arrive at the classic TW84 result

$$\mathcal{T}_N^{\text{TW84}} = 0. \quad (56)$$

This zero torque result is a consequence of the symmetry of the dark matter density distribution that arises when the DF completely phase mixes within and around the resonant island. Simply put, in the fully phase-mixed state, there are the same number of particles “pushing” on the bar as “pulling” on it; see Figures 4, 7, and 16 of Chiba & Schönrich (2022) for illustration.

The linear and nonlinear torque calculations pursued by the above authors (LBK; Weinberg 2004; TW84; Chiba & Schönrich 2022) and similar efforts by others (Weinberg 1989; Kaur & Sridhar 2018; Banik & van den Bosch 2021, 2022; Kaur & Stone 2022) were all collisionless; their DF f only responded to the smooth combined potential of the underlying equilibrium galaxy Φ_0 and the rigidly rotating perturbation $\delta\Phi$, in effect setting $\Delta = 0$. The only related (semi-)analytical study we know of to have included the effects of diffusion ($\Delta > 0$) in this problem is Weinberg & Katz (2007a), but their focus was on the evolution of the bar pattern speed and the associated rate at which resonances sweep through phase space (see Section 5.2). In the remainder of this section, we will investigate how finite Δ affects the dynamical friction torque on galactic bars, focusing on the corotation resonance $N = (0, 2, 2)$ identified as dominant by Chiba & Schönrich (2022).

4.3. The Corotation Torque Density

We want to calculate the torque on the bar using the nonlinear torque Equation (55) and substituting for f our solution to the kinetic equation discussed in Section 3.2, for different values of Δ . Following Chiba & Schönrich (2022), we use as our dark matter halo model the Hernquist sphere (1), and we take our unperturbed dark matter DF $f_0(\mathbf{J})$ to be the isotropic Hernquist DF (Hernquist 1990). In Figure 7, we show colored contours of $f_0(L, J_r)$ at fixed (arbitrary) inclination:

$$\beta \equiv \arccos(L_z/L). \quad (57)$$

For our bar potential, we use the model (2)–(3), with the choices of numerical parameters given below Equation (3). We will focus only on the corotation resonance $N = (0, 2, 2)$, so the implicit equation for the resonant line in phase space is

$$\Omega_\psi(L, J_r) = \Omega_p, \quad (58)$$

with $\Omega_p = 35 \text{ km s}^{-1} \text{ kpc}^{-1} = 35.8 \text{ Gyr}^{-1}$. We plot this resonant condition with a solid black line in Figure 7. We also choose two particular resonant locations, shown with black dots, corresponding to $J_r = 500 \text{ kpc}^2 \text{ Gyr}^{-1}$ and $J_r = 50 \text{ kpc}^2 \text{ Gyr}^{-1}$, respectively, and we will refer to these momentarily.

Next, given the choice of N , it follows from (11)–(12) that

$$\mathbf{J}_f = (J_r, L(1 - \cos \beta)), \quad (59)$$

$$J_s = \frac{L \cos \beta}{2}, \quad (60)$$

Thus, at fixed inclination, L is (proportional to) the slow action, while J_r is a fast action. Let us suppose the bar is initially absent and the DF is $f_0(\mathbf{J})$, and then at $t = 0$ we suddenly turn on the bar perturbation. Particles that were initially on zero-inclination orbits in the background spherical potential ($\beta = 0$) will remain at zero inclination even under the finite bar perturbation, which follows from the conservation of the fast action J_{f2} (Equation (59)). As a result, for these particles, L is a genuine slow action (up to a factor of 2), meaning they move in the (L, J_r) phase space only along the horizontal lines of constant J_r —for instance, along one of the black dotted horizontal lines shown in Figure 7. Ignoring diffusion for now, particles that are initially sufficiently close to the resonance will be trapped by it and will oscillate back and forth across the solid black resonant line (librating orbits). Particles that are somewhat further away from the resonance will also oscillate in L but will not cross the resonant line (circulating orbits).

Before we proceed with our torque calculation, one conceptual hurdle must be overcome. Namely, for a given diffusion coefficient D , the corotation torque $\mathcal{T}_{(0,2,2)}^{\text{nl}}(t)$ involves contributions from a range of different Δ values. To demonstrate this, in Figure 7 we show the extent in j of the librating orbits (i.e., the resonance width) for $\beta = 0$ with red bars; in other words, these red bars correspond to $j \in (-2, 2)$. We notice that the resonance width depends on the choice of J_r . Similarly, with the yellow bars in Figure 7, we show the resonance width for the same J_r values but a different inclination, namely $\beta = \pi/2$, and again the width changes.¹⁰ Moreover, it is easy to show that the libration time t_{lib} depends

¹⁰ There is a minor subtlety here: for orbits that are initially at nonzero inclination, the inclination precesses under the bar perturbation, so the action-space evolution of an initially inclined particle cannot be fully captured in a single $\beta = \text{constant}$ diagram. Regardless, the width of the resonance clearly depends on β .

on both β and J_r . It follows that Δ (Equation (29)) is not a constant but rather a function of (J_r, β) . The corotation torque $\mathcal{T}_{(0,2,2)}^{\text{nl}}(t)$ involves an integration over L , J_r , and $\cos \beta$ (see Equation (55)), and therefore has contributions from many different Δ . Because our purpose in this paper is to understand how the physics of resonances depends on Δ (rather than to provide the most accurate possible computation of the frictional torque), we choose to isolate a quantity that involves only a single value of Δ . This quantity is the corotation torque density \mathcal{S} , defined such that

$$\mathcal{T}_{(0,2,2)}^{\text{nl}}(t) = \int dJ_r d\cos \beta \mathcal{S}(t|J_r, \cos \beta). \quad (61)$$

Thus, $\mathcal{S}(t)$ measures the contribution to the total corotation torque from dark matter particles with radial actions $\in (J_r, J_r + dJ_r)$ and inclinations $\in (\cos \beta, \cos \beta + d\cos \beta)$. Importantly, for a fixed J_r and $\cos \beta$, the torque density \mathcal{S} has contributions from only a single value of Δ , which we are therefore free to stipulate by hand.

The formula for \mathcal{S} turns out to be

$$\mathcal{S}(t|J_r, \cos \beta) = 2(2\pi)^3 \int dL L \Psi_1 \text{Im} f_1, \quad (62)$$

where (Chiba & Schönrich 2022, Appendix B):

$$\Psi_1(\mathbf{J}) = \frac{(1 + \cos \beta)^2}{8\pi} \int_0^\pi d\theta_r \Phi_b(r) \cos[2(\theta_\psi - \psi)]. \quad (63)$$

For a given Δ value and choice of $(J_r, \cos \beta)$, we can compute $\text{Im} f_1$ using the numerical solution to the kinetic Equation (30) that we described in Section 3, setting the initial condition to be of the form (36) by linearizing the isotropic Hernquist DF (shown in Figure 7) around the resonance. We can also calculate $\Psi_1(\mathbf{J})$ (Equation (63)) efficiently on a grid in $(L, J_r, \cos \beta)$ space using the standard mappings for $(\mathbf{x}, \mathbf{v}) \rightarrow (\boldsymbol{\theta}, \mathbf{J})$ for spherical potentials (e.g., Section 3.5.2 of Binney & Tremaine 2008) and the “angular anomaly” trick from Appendix B of Rozier et al. (2019). As mentioned below Equation (54), when performing the integral in (62) one has to choose the maximum/minimum L (or equivalently, j) values at which to cut it off, and this choice will affect the results, as we will see.

4.4. Results

In this section, we present the results of our corotation torque density calculations for various Δ . A reader uninterested in the details can skip to the summary in Section 4.4.1.

In Figure 8, we show the bar’s dimensionless slowing rate

$$\mathcal{S}(t)/\mathcal{S}_{\text{LBK}}, \quad (64)$$

where \mathcal{S}_{LBK} is the **LBK** corotation torque density (see Equation (52)):

$$\begin{aligned} \mathcal{S}_{\text{LBK}}(J_r, \cos \beta) &= 4(2\pi)^3 \int dL L |\Psi_1|^2 \frac{\partial f_0}{\partial L} \\ &\times \pi \delta[2(\Omega_\psi - \Omega_p)], \end{aligned} \quad (65)$$

which is the result of computing the torque density using linear theory with $\Delta = 0$. In each panel, we fix the inclination $\beta = 0$ and radial action $J_r = 500 \text{ kpc}^2 \text{ Gyr}^{-1}$, so the resonance location corresponds to the upper black dot in Figure 7. The libration timescale (Equation (20)) for this resonance location is $t_{\text{lib}} = 1.9 \text{ Gyr}$. In each panel of Figure 8, we plot the slowing

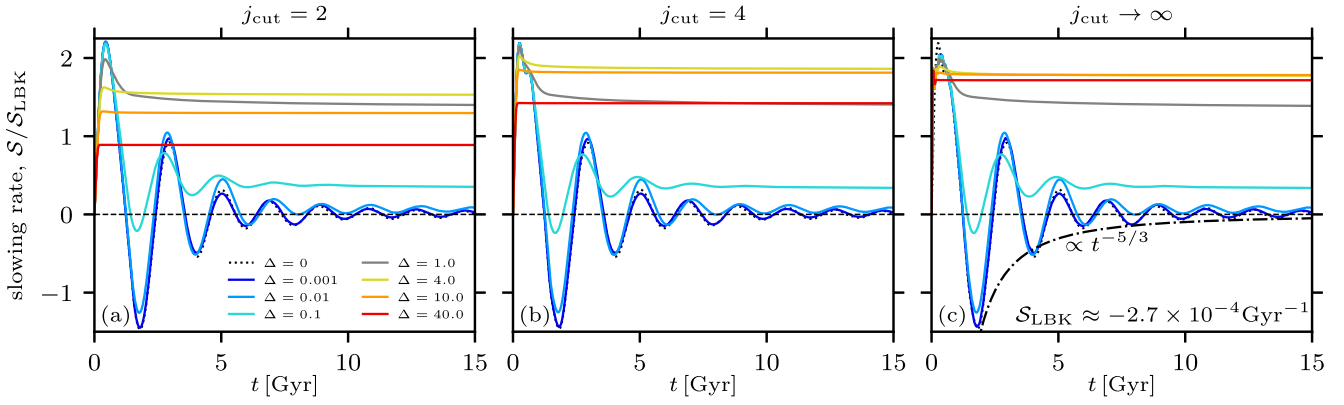


Figure 8. Dimensionless slowing rate of the bar $\mathcal{S}(t)/\mathcal{S}_{\text{LBK}}$ due to halo friction, specifically from dark matter particles with $\beta = 0$ and $J_r = 500 \text{ kpc}^2 \text{ Gyr}^{-1}$. The libration time is $t_{\text{lib}} = 1.9 \text{ Gyr}$ and the **LBK** corotation torque density is $\mathcal{S}_{\text{LBK}} = -2.7 \times 10^{-4} \text{ Gyr}^{-1}$. Colored lines show results for different $\Delta > 0$, while the dotted line shows the collisionless ($\Delta = 0$) result. In panels (a)–(c), we cut off the integral in (62) at $j_{\text{cut}} = 2, 4$ and ∞ , respectively.

rate (64) for various values of $\Delta \geq 0$. It should be noted that \mathcal{S}_{LBK} is negative, so that a positive value of $\mathcal{S}(t)/\mathcal{S}_{\text{LBK}}$ means the bar feels a negative torque (slowing it down). The difference between the panels lies in our choice of integration limits in Equation (62): we choose the limits to be $j = \pm j_{\text{cut}}$ for $j_{\text{cut}} = 2, 4$ and ∞ in panels (a)–(c), respectively.¹¹ It should also be noted that \mathcal{S}_{LBK} (Equation (65)) does not depend on j_{cut} .

Let us focus first on panel (a), which is for $j_{\text{cut}} = 2$, meaning that the edges of our integration domain just graze the maximum extent of the separatrix in the (ϕ, j) plane. In the collisionless case ($\Delta = 0$, black dotted line), we see that the slowing rate oscillates on the timescale $\sim t_{\text{lib}}$. This is the same behavior as found by Chiba & Schönrich (2022)—indeed, the $\Delta = 0$ results shown here are very similar to the top panel of their Figure 11.¹² The envelope of the $\Delta = 0$ curve decays approximately as $\propto (t/t_{\text{lib}})^{-5/3}$ (shown explicitly in panel (c)), so in the time-asymptotic limit for $\Delta = 0$, we recover the TW84 result (see Equation (56)),

$$\mathcal{S}(t \rightarrow \infty) = 0, \quad (\Delta = 0), \quad (66)$$

which follows from the symmetry of the fully phase-mixed DF in slow angles, i.e., $\text{Im } f_1(j, \tau \rightarrow \infty) = 0$ (Figure 5). However, as one deviates from $\Delta = 0$ to finite (but small) $\Delta > 0$, the behavior changes. The steady state is reached sooner than it was in the collisionless case, following our expectations from Section 3.3.2. In addition, the slowing rate in the steady state is manifestly positive for all $\Delta > 0$. This is a consequence of the fact that, while phase mixing attempts to abolish the asymmetry of the slow-angle distribution, diffusion replenishes it (e.g., Figure 2(b)) leading to a finite $\text{Im } f_1$ (Figure 5). Indeed, the slowing rate in Figure 8 grows with Δ until, for $\Delta \sim 1$, it is actually larger than the **LBK** value. This growing trend continues up to around $\Delta \sim 10$, when the slowing rate starts to decay with increasing Δ , albeit rather gradually; even by $\Delta = 40$, the steady-state slowing rate is barely smaller than the **LBK** prediction.

This story mostly repeats itself in panels (b) and (c), i.e., for $j_{\text{cut}} = 4$ and $j_{\text{cut}} \rightarrow \infty$, respectively, with some key differences.

First of all, the transient early-time behavior of the slowing rate ($t < t_{\text{lib}}$) is sensitive to the choice of j_{cut} , especially for small Δ , as might be expected, e.g., from the first two panels of Figure 2(a). Yet for $t \gtrsim t_{\text{lib}}$, the $\mathcal{S}(t)$ curves for small $\Delta \lesssim 1$ in Figure 8 take a near-universal form independent of j_{cut} . This is because, for $\Delta \lesssim 1$, the steady-state value of $\text{Im } f_1(j)$ is negligible outside of the separatrix region $j \in (-2, 2)$ (see Figure 5). Physically, under very weak diffusion, the disturbances to the initial DF produced by the bar cannot propagate very far beyond the resonant island (as reflected in, e.g., Figure 3(c)), so it is not possible to produce angular asymmetries at large j . This renders the slowing rate insensitive to j_{cut} as long as one chooses a value larger than about 2. Essentially the same conclusion was drawn by Chiba & Schönrich (2022) when they noted that the great majority of the torque in the collisionless limit came from trapped orbits as opposed to circulating ones. On the other hand, in the strong-diffusion limit $\Delta \gg 1$, the slowing rate is sensitive to j_{cut} , because disturbances are able to propagate much further. Mathematically, for $\Delta \gg 1$, the curve of $\text{Im } f_1(j, \tau \rightarrow \infty)$ becomes very broad in j , with a width $\propto \Delta^{1/3}$; see Section 3.3.4.

To make this analysis more quantitative, in Figure 9 we plot the steady-state value of the slowing rate as a function of Δ , again for $j_{\text{cut}} = 2, 4, \infty$. We see that, at the low- Δ end, the steady-state slowing rate closely follows the scaling $\propto \Delta^{4/5}$, irrespective of j_{cut} . This reflects the fact that, for small Δ , the width of the $\text{Im } f_1$ curve is approximately independent of Δ (Figure 5), while its amplitude scales like $\propto \Delta^{4/5}$ (Figure 6(b)). Meanwhile, at the high- Δ end in Figure 9, the steady-state slowing rate decays as $\propto \Delta^{-1/3}$ for $j_{\text{cut}} = 2$ but approximately converges toward a constant for $j_{\text{cut}} \rightarrow \infty$. This can be understood as follows. By cutting off the integral in (62) at $j = \pm 2$, we render the steady-state torque sensitive only to the height—and not the width—of the $\text{Im } f_1$ curve, and we know from Equations (46)–(47) and Figure 6(b) that this height scales like $\Delta^{-1/3}$. But by extending the domain of integration out to infinity, we are able to count all contributions to $\text{Im } f_1$; and because we know from Section 3.3.4 that $\int_{-\infty}^{\infty} dj \mathcal{R}_{\Delta}(j) = 1$ is independent of Δ , it is unsurprising that the torque converges for large Δ . The interested reader may refer to Section 5.2 for further discussion.

In Figure 10, we repeat the same calculation as in Figure 8(b) except this time for a much smaller radial action $J_r = 50 \text{ kpc}^2 \text{ Gyr}^{-1}$, so the resonance location corresponds to the lower black dot in Figure 7. The libration timescale in this case is shorter,

¹¹ Really, the third value is $j_{\text{cut}} = 10$, but this is essentially indistinguishable from $j_{\text{cut}} \rightarrow \infty$. Also, when $-j_{\text{cut}}$ corresponds to a negative L , we set the minimum j to whichever value corresponds to $L = 0$.

¹² However, they plot the total corotation torque $-\mathcal{T}_{(0,2,2)}$ (Equation (61)), whereas we only plot the corotation torque density (62).

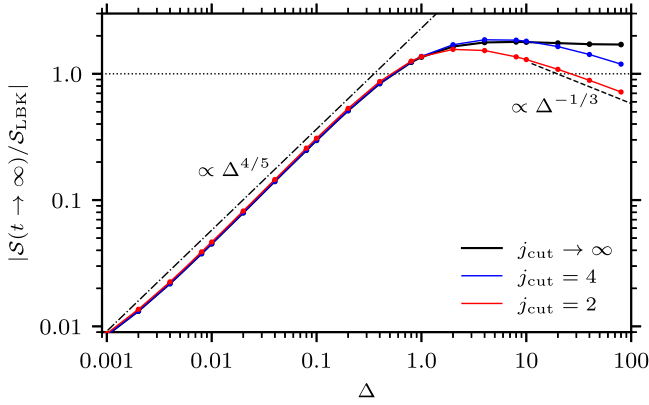


Figure 9. Steady-state value of $\mathcal{S}(t)/\mathcal{S}_{\text{LBK}}$ as a function of Δ (both axes are on a logarithmic scale). We show the results for the same choice of resonance location as in Figure 8, computed with the cutoffs $j_{\text{cut}} = 2, 4, \infty$.

$t_{\text{lib}} = 1.3$ Gyr. Though we are now considering dark matter particles that are typically on much more circular orbits than in Figure 8(b), the results we find are remarkably similar. The key differences are that, in Figure 10, the amplitude of the slowing rate is almost an order of magnitude larger, which reflects the larger value of $|L\Psi_1|$ for these more circular orbits, and its oscillation period is shorter, owing to the shorter libration time. For small Δ , apart from these rescalings, there is almost no difference from the results of Figure 8(b). This again follows from the fact that, for weakly diffusive systems, $\text{Im} f_j$ tends to be negligible outside of $j \in (-2, 2)$. We can show that the factor Ψ_1 does not vary much over this range, meaning it can be approximated by a constant in (62), and the only remaining J_{res} dependence in (62) lies in the overall prefactor and in the scaling of the time coordinate $\tau = 2\pi t/t_{\text{lib}}(J_{\text{res}})$.

Which value of j_{cut} is the physically relevant one? This is actually a nontrivial question, because in a detailed calculation one would need to consider all important resonances N , then look carefully at the volume of phase space dominated by the corotation resonance and choose j_{cut} so that the domain of integration does not extend beyond this volume (Chiba & Schönrich 2022). Moreover, even if corotation was the only important resonance, we could still not fully justify taking $j_{\text{cut}} \rightarrow \infty$ here because throughout this paper we used the simplification that the background DF $f_0(J)$ could be linearized around the resonance location (Equation (36)). It is clear from Figure 7 that, as we venture far from the resonance, this linear approximation becomes a very poor one. We could, of course, generalize our results to more realistic initial conditions (Pao 1988), but this is beyond the scope of this paper. Also, far from the resonance, the pendulum approximation (17) eventually breaks down.

Nevertheless, regardless of the choice of j_{cut} , we see from Figure 9 that the steady-state torque density for $J_r = 500 \text{ kpc}^2 \text{ Gyr}^{-1}$ and $\beta = 0$ (the upper resonant location in Figure 7) is comparable to the LBK value (65) over the entire range $\Delta \in (1, 100)$, and it scales robustly as $\propto \Delta^{4/5}$ for small Δ . Although not shown here, equivalent plots using $J_r = 50 \text{ kpc}^2 \text{ Gyr}^{-1}$ (the lower resonance in Figure 7), as well as other choices of J_r , show very similar results. We also note that performing these calculations again for different values of $\beta \neq 0$ gives qualitatively the same results. (However, as mentioned in Section 4.3, the interpretation of such results is more subtle because, for $\beta \neq 0$, the orbital inclination precesses, meaning the

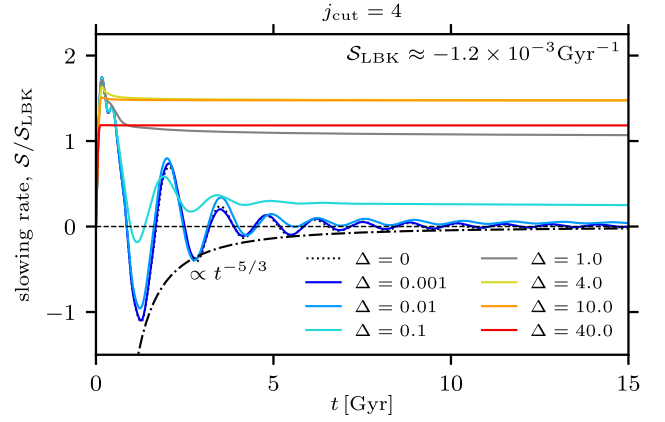


Figure 10. As in Figure 8, except for $J_r = 50 \text{ kpc}^2 \text{ Gyr}^{-1}$ and showing only the results for $j_{\text{cut}} = 4$.

particles with inclination β at time t are not the same particles that were at inclination β at time $t - \delta t$.)

4.4.1. Summary of This Section

The key result of this section is that the corotation torque density is very sensitive to Δ at the small- Δ end, growing almost linearly with Δ , but it is much less sensitive for large Δ , and for $\Delta \gtrsim 1$, the LBK torque is a robust estimate. More quantitatively, we suggest the following heuristic fitting formula for the corotation torque density:

$$\mathcal{S}(t \rightarrow \infty) \sim \min(\Delta^{4/5}, 1) \times \mathcal{S}_{\text{LBK}}. \quad (67)$$

Alternatively, a reasonable fit to the $j_{\text{cut}} \rightarrow \infty$ curve in Figure 9, accurate to within a few tens of percent over all five decades in Δ , is $\mathcal{S}(t \rightarrow \infty)/\mathcal{S}_{\text{LBK}} = 2\Delta^{4/5}/(1 + \Delta^{4/5})$.

We discuss the astrophysical implications of our results on bar-halo friction in Section 5.2.

5. Discussion

Bar resonances are key drivers of the secular evolution of galaxies. However, analytical studies and test-particle simulations of dynamical interactions between a bar and a population of stars or dark matter particles are often highly idealized, in the sense that they are collisionless; they only consider the evolution of particle distribution functions (DFs) in smooth prescribed potentials, ignoring the diffusive effects of passing stars, molecular clouds, dark matter substructure, transient spiral waves, etc. Meanwhile, N -body simulations presumably capture (at least some of) this diffusive physics, but they are difficult to interpret and are rarely linked back quantitatively to the underlying dynamical processes. Moreover, N -body simulations themselves inevitably include some level of numerical diffusion, even if they purport to describe a perfectly collisionless system (Weinberg 2001; Weinberg & Katz 2007a; Sellwood 2013; Ludlow et al. 2019, 2021).

In this paper, we have taken a step toward reconciling these various approaches by developing a kinetic framework that accounts for both a secular driving of the DF by a rigidly rotating bar perturbation and a generic diffusion in the associated slow action variable. The kinetic equation we proposed is the simplest possible one that allows us to move beyond the paradigmatic collisionless calculations of Lynden-Bell & Kalnajs (1972), Tremaine & Weinberg (1984), Binney (2016), etc. In its dimensionless form (Equation (30)), the

kinetic equation depends on a single dimensionless parameter, the diffusion strength Δ (Equation (29)). All past collisionless models have implicitly set $\Delta = 0$, but in stellar disks we can easily have $\Delta \sim 1$, and Δ can also be significantly different from zero in the dark matter halo, depending on the form that the dark matter takes, suggesting that some of the conclusions drawn from collisionless models may need to be revised.

In the remainder of this section, we first mention various limitations of the model we have developed here (Section 5.1). We then discuss the implications of our results for studies of bar–halo friction (Section 5.2), describe the connection between this work and various seminal studies in plasma physics (Section 5.3), and conclude by discussing future directions (Section 5.4).

5.1. Limitations of This Work

Our purpose here has not been to provide a detailed model of the bar-driven evolution of the Milky Way (or any other galaxy), but rather to elucidate some theoretical ideas upon which future detailed models may be based. Though we believe we have succeeded in this aim, our model is certainly an unrealistic portrayal of any real galactic bar. For example, we have assumed that the bar’s resonances are well-separated in phase space so that there is little resonance overlap. This seems to be a reasonable assumption for dark matter trapping (Chiba & Schönrich 2022), but it is probably not the case for stars in the Galactic disk, where resonance overlap is a significant contributor to transport (Minchev & Famaey 2010; Minchev et al. 2012). We have also assumed throughout that the bar is a rigidly rotating structure with constant pattern speed and strength. Even in our dynamical friction calculations, we have not accounted for the fact that the friction causes the pattern speed to change, which in turn causes the resonance locations to sweep through action space. We discuss this further in Section 5.2. Moreover, many simulations show that the bar parameters actually fluctuate with time (Fujii et al. 2018); recently, Hilmi et al. (2020) simulated two Milky Way–like galaxies and found that both bar pattern speed and strength fluctuate at the level of 10%–20% on orbital timescales (~ 100 Myr), mostly due to interactions with spiral arms. One can show that fluctuations in the pattern speed and/or strength of the bar causes an effective diffusion of particle orbits (though not precisely as a random walk in J_s). Heuristically, therefore, one might guess that inclusion of fluctuating bar parameters amounts to little more than an increased effective Δ . We leave a careful study of this problem to future work.

Another major assumption we have made throughout the paper is that there is no diffusion of particles’ fast actions J_f . This assumption is not fully justifiable in the general case—for example, local isotropically distributed scattering events should produce diffusion in all three action variables, not just the slow variable J_s . It is worth mentioning that the same assumption is made implicitly in collisionless models. In fact, in collisionless models, a distinct phase space island exists at every J_f , and the DF phase mixes perfectly within this island, similarly to Figure 2(a), with no crosstalk between different J_f values. This becomes problematic when even a small amount of diffusion is included, because the phase-mixed island structures at each J_f inevitably produce sharp gradients of f in the J_f direction, because the location and shape of the resonant island changes as a function of J_f (for instance, $J_{s, \text{res}}$ itself is a function of J_f through Equation (8), and we already argued that the width of the resonance depends on J_f in Section 4.3). Because of these

sharp gradients, a diffusive term like $\sim \partial^2 f / \partial J_f^2$ in the kinetic equation is liable to become large, and hence J_f diffusion will start to “fill in” the flattened regions in the DF produced by phase mixing.¹³ This suggests that, in reality, the effective Δ is again higher than one would naively estimate based on Equation (32). Nevertheless, our study is still useful in that it allows us to quantify, even if only roughly, the impact of stochastic effects upon resonant structures through a single intuitive parameter Δ . If the aforementioned complications do indeed increase the effective Δ , this will only reinforce our main point that, in many astrophysically relevant scenarios, diffusive effects cannot be ignored.

We also neglected to include any drag term in our collision operator (24), which is usually valid as long as the scattering agents (molecular clouds, spiral arms, etc.) are sufficiently massive compared to the particles in question (Binney & Lacey 1988). However, drag can be an important ingredient if, for instance, f were to describe heavy bodies (e.g., MACHOs) or a population of stars in a tepid disk (Fouvry et al. 2015). In this case, resonance lines, in addition to experiencing broadening, are predicted to shift and split (Duarte et al. 2023).

5.2. Bar–Halo Friction

The primary application of our study is to the problem of bar–halo friction (Section 4). This topic has provoked significant controversy in the literature, both among theoreticians (Debattista & Sellwood 2000; Weinberg & Katz 2007a; Sellwood 2008; Athanassoula 2013) and among simulators and observers, who argue about possible tensions in Λ CDM cosmology (Fragkoudi et al. 2021; Roshan et al. 2021; Frankel et al. 2022). Let us discuss what our results do, and do not, imply about this problem.

First, we emphasize that we have not actually calculated the frictional torque at all, but only the corotation torque density at fixed J_r and β . Astrophysical inferences from our results are therefore necessarily an extrapolation, although we take confidence from the fact that our torque density results for $\Delta = 0$ do resemble closely the full torque calculations of Chiba & Schönrich (2022). We have also not considered halos either with spin or with anisotropic velocity distribution functions, and altering these characteristics may change the bar–halo friction significantly (e.g., Li et al. 2022). For instance, the corotation torque will be much reduced in a radially anisotropic halo (compare the LBK values in Figures 8 and 10), but the Lindblad resonances might become relatively more important.

Despite these major caveats, suppose we take the formula (67) to be a broadly correct description not only of the corotation torque density, but of the dynamical friction torque as a whole: that is, we replace $\mathcal{S} \rightarrow \mathcal{T}$ and reinterpret the (strictly local, J_f -dependent) diffusion strength Δ as some characteristic value, perhaps averaged over the important regions of phase space. Then our results suggest that real galactic bars will always feel some nonzero torque, because finite diffusion will always replenish some asymmetry in the angular distribution of the particles as viewed in the bar frame. Our results also suggest that, for systems with moderate to strong diffusion ($\Delta \gtrsim 1$), the LBK formula provides a robust order-of-magnitude estimate of the frictional torque. Further, for $\Delta \lesssim 1$, the time-asymptotic

¹³ The longitudinal plasma wave calculation of Pao (1988) did include three-dimensional diffusion, but he had the advantage of working in velocity space rather than action space, which simplifies the calculations significantly, and it is not clear whether a comparable angle-action calculation could be developed.

torque grows almost linearly with Δ , meaning that in some cases a relatively collisional component of a galaxy (e.g., the stellar disk for which $\Delta \sim 1$; see Section 3.1) might make a significant contribution to the torque, even though it carries much less mass than the nearly collisionless cold dark matter halo (for which $\Delta \ll 1$).

The fact that the **LBK** torque formula provides a good order-of-magnitude estimate for any $\Delta \gtrsim 1$ can be understood as follows (see also Johnston 1971). Physically, diffusion tends to render the bar-particle interaction problem linear in the sense that particles are never truly trapped by the bar—for instance, they never undergo a full libration around the origin in the (ϕ, j) plane (Figure 2) before being kicked to a new j value outside of the resonant island. In other words, when diffusion dominates over libration, particle trajectories are well-described in the original angle-action variables (θ, J) , and they approximately consist of the unperturbed motion ($J = \text{const}$, $\theta \propto \Omega t$) punctuated by frequent instantaneous jumps in J . This means that one can calculate the dynamical friction torque using the same linear perturbation techniques as in the collisionless **LBK** theory (Section 4.1), while accounting for the additional diffusion. The effect of this additional ingredient is basically to broaden the resonance line in action space, so that the δ -function encoding exact resonances in the **LBK** formula (65) gets replaced by the function \mathcal{R}_Δ (Equation (47)). But because the “integral under the line” of this broadened resonance function is always unity regardless of Δ , the torque we calculate in the broadened case does not differ much from the **LBK** result. More quantitatively, using the identity $\int_{-\infty}^{\infty} dx p(x) \delta(q(x)) = p(x_0)/|q'(x_0)|$, where x_0 is assumed to be the lone zero of $q(x)$, we can rewrite the **LBK** formula (65) as

$$\mathcal{S}_{\text{LBK}} = (2\pi)^4 \left(L |\Psi_1|^2 \frac{\partial f_0}{\partial L} \bigg/ \left| \frac{\partial \Omega_\psi}{\partial L} \right| \right)_{\text{res}}, \quad (68)$$

where the subscript “res” indicates that everything inside the bracket is to be evaluated on resonance. Next, let us crudely approximate the integrand of the nonlinear torque (62) with its resonant value and “perform the integral” by multiplying this with some resonance width δL . Comparing the result with (68), using the fact that, for our choice of slow actions, $(\partial \Omega_\psi / \partial L)_{\text{res}} = G/4$ and $(\partial f_0 / \partial L)_{\text{res}} = \alpha/I_h$, and employing the definitions (18) and (21), one can show that

$$\frac{\mathcal{S}(t \rightarrow \infty)}{\mathcal{S}_{\text{LBK}}} \approx \frac{2}{\pi} \frac{\delta L}{I_h} \text{Im } g_1(0). \quad (69)$$

We know from Section 3.3.4 that, for large Δ , the resonance width is $\delta L \sim \Delta^{1/3} I_h$ and $\text{Im } g_1(0) \sim \Delta^{-1/3}$. It follows that, as long as $\Delta \gtrsim 1$, we always have $\mathcal{S}(t \rightarrow \infty)/\mathcal{S}_{\text{LBK}} \sim 1$.

We note that the above argument does not hold in the $\Delta < 1$ regime, in which trapped orbits typically do undergo at least one full libration before being kicked out of resonance. In this regime, the “resonance function” takes on a qualitatively different form—indeed, one can see from Figure 5 that the “area under the curve” of $\text{Im } g_1$ is not close to a constant for small Δ values.

Conclusions similar to these were also reached by Weinberg & Katz (2007a), who considered the effect of finite particle number upon simulations of bar-halo coupling. They derived criteria for the minimum particle number N_{crit} required such that a simulation might faithfully reproduce the collisionless (TW84) dynamics, rather than destroying the nonlinear trapping effects

by spurious numerical diffusion.¹⁴ In our language, they were trying to determine the minimum number of particles N that would still produce $\Delta \ll 1$ (see Equation (35)). However, as Weinberg & Katz (2007a) noted, the time-asymptotic TW84 limit (56) may never be reached even in a genuinely collisionless ($\Delta = 0$) system if the pattern speed of the bar, Ω_p , is allowed to change self-consistently, because this will cause the resonance location to sweep through phase space. In particular, if Ω_p changes fast enough that the resonance sweeps past new halo material on a timescale that is short compared to t_{lib} —the so-called “fast limit” (see TW84)—then nonlinear librations never occur and the torque on the bar is approximated well by linear (**LBK**) theory.¹⁵ On the other hand, this trend can be halted if Ω_p evolves nonmonotonically (Sellwood & Debattista 2006). In particular, if a gently slowing bar experiences a small positive fluctuation in Ω_p , the resonances responsible for friction will be nudged “back” to the phase space locations they just came from. At these locations, the gradient in the distribution function will have been flattened. This will lead to an anomalously small frictional torque relative to the **LBK** value, helping to keep the bar in the slow regime (what Sellwood & Debattista 2006 call a “metastable” state).

Two key points emphasized by Weinberg & Katz (2007a) were as follows. (i) Even if the real system one wishes to simulate genuinely does lie in the “slow limit” where nonlinear trapping is crucial, a finite- N simulation of this system with too much numerical diffusion may produce evolution in the fast limit. Our results are consistent with this idea: increasing the diffusion strength Δ from a small value $\ll 1$ tends to increase the frictional torque. (ii) If a simulation employs far too few particles, $N \ll N_{\text{crit}}$, then a simple convergence study in N may be misleading. In the language of our paper, the reason for this is that if the initial simulation had $\Delta \gg 1$, then, e.g., a tenfold increase in N will only lead to a tenfold decrease in Δ . If such a decrease still leaves $\Delta > 1$, then we know from Figure 9 that one will measure almost precisely the same torque again, so the numerics will appear converged. In other words, one may need to increase N much further, with no apparent change in the measured torque $\mathcal{T}(N)$ until it eventually changes discontinuously around $N \sim N_{\text{crit}}$ (corresponding to $\Delta \sim 1$). Our Figure 9 helps to illustrate and quantify both points (i) and (ii), but a proper study with time-dependent Ω_p and a very wide range of effective particle numbers is required to make these claims precise (Sellwood 2008). In particular, the mechanism from Sellwood & Debattista (2006) described above is a particularly sensitive test case; the ability of a simulation to reproduce this effect would be a reassuring sign (though not a guarantee) that particle number requirements are being met.

Finally, we should not forget that there are many decades in Δ that lie between the TW84 ($\Delta = 0$) and **LBK** ($\Delta \gtrsim 1$) limits, especially because it is in this regime that most cosmological simulations probably sit (Section 3.1). Indeed, even $\Delta \sim 0.1$ can lead to a significant bar slowdown over a Hubble time, and such values are plausible even in simulated halos that are naively converged, i.e., those with two-body relaxation times $\gg 10$ Gyr. Further work along the lines of Sellwood (2013), Ludlow et al. (2019, 2021), and Wilkinson et al. (2023) will be needed to confirm the extent to which bar slowdown is driven by spurious

¹⁴ As well as satisfying certain “numerical coverage” criteria that we will not discuss here.

¹⁵ Or rather, the time-dependent version of **LBK** theory; see Equation (51) and Weinberg (2004).

Table 1
Guide to Some Complementary Papers in the Analytic Theory of Wave

| | Collisionless | Collisional |
|---|---|---|
| Linear theory | Landau (1946) Lynden-Bell & Kalnajs (1972) Weinberg (2004) | Auerbach (1977) Catto (2020) |
| Nonlinear theory (w/particle trapping) | $\Delta = 0$ Mazitov (1965), O’Neil (1965) Tremaine & Weinberg (1984) Chiba & Schönrich (2022) | $0 < \Delta \ll 1$ Pao (1988) Petviachvili (1999) $\Delta \gg 1$ Berk et al. (1997) Duarte & Gorelenkov (2019) <—This paper (Hamilton et al. 2023)—> |

Notes. Particle interactions in plasma kinetics (shown in regular text) and galactic dynamics (shown in bold). We split the papers by whether the authors considered the linear or the nonlinear response of the particle DF to the wave perturbation, and whether their calculation did or did not include diffusion. The present paper belongs in the lower-right quadrant.

numerical noise. Our results also suggest that alternative dark matter models such as fuzzy dark matter (Hui et al. 2017) may produce different bar–halo friction signatures, potentially constraining cosmological models (e.g., Debattista & Sellwood 1998; Lancaster et al. 2020).

5.3. Relation to Plasma Literature

A note is warranted here on the many correspondences between stellar-dynamical and plasma-kinetic theory. Our kinetic Equation (30) turns out to be mathematically identical to an equation employed in a range of plasma-kinetic calculations of wave–particle interactions (Pao 1988; Berk et al. 1997; Duarte et al. 2019). However, we have not seen it expressed in this dimensionless single-parameter form before, nor have we seen the solutions examined so closely as in Section 3.2, meaning our results may be of use for future plasma studies. The plasma literature more generally is replete with analyses of nonlinear particle trapping, diffusive resonance broadening, and so on (e.g., Dupree 1966; Su & Oberman 1968; Ng et al. 2006; Black et al. 2008; White & Duarte 2019; Catto 2020; Catto & Tolman 2021; Tolman & Catto 2021). Moreover, the LBK formula (52) is directly analogous to the classic formula for the Landau damping rate of a Langmuir wave in an electrostatic plasma (Landau 1946; Ichimaru 1965) or Landau damping in more general geometry (Kaufman 1972; Nelson & Tremaine 1999). The TW84 calculations that account for nonlinear trapping of particles in resonances are strongly analogous to the “nonlinear Landau damping” calculations by Mazitov (1965) and O’Neil (1965) (who unsurprisingly found that the damping/growth rate of waves goes to zero in the fully phase-mixed limit). In a similar vein, the calculations in the present paper are analogous to those works that have attempted to combine O’Neil’s and Mazitov’s calculation with a simple model for interparticle collisions (e.g., Zakharov & Karpman 1963; Pao 1988; Brodin 1997). The approximate recovery of the LBK torque from the nonlinear torque in the large $\Delta \gg 1$ limit is closely related to the recovery of the Landau damping formula from the O’Neil/Mazitov formula (Johnston 1971; Auerbach 1977). In Table 1, we provide a summary guide to this plasma-kinetic/stellar-dynamical correspondence and show where the present paper fits into the literature.

5.4. Outlook and Future Work

In recent years, our analytic understanding of dynamical friction in the collisionless ($\Delta = 0$) limit has been greatly

improved, e.g., by the work of Banik & van den Bosch (2021), Banik & van den Bosch (2022), Chiba & Schönrich (2022), Kaur & Sridhar (2018), and Kaur & Stone (2022). To some extent, these authors have advocated an “orbit-based” interpretation of dynamical friction. For instance, Chiba & Schönrich (2022) and Banik & van den Bosch (2022) calculated the contributions to the friction from individual particles at different points in their orbits, compared the torque coming from trapped orbits to those from untrapped orbits, and so on. Our finite- Δ calculations show the benefit of a complementary viewpoint, in which dynamical friction is a kinetic process—something that needs to be understood primarily in terms of distribution functions as opposed to individual particle trajectories. In reality, no particle is permanently trapped or untrapped by a resonance, because for finite Δ , there is a constant flux of particles into and out of the librating region, even in a steady state.

The most obvious extension of the current work is to a system in which the bar pattern speed Ω_p is decaying monotonically (Weinberg & Katz 2007a, 2007b; Sellwood 2008). We must also quantify carefully the impact of diffusion in fast actions J_f , and calculate the full torque by integrating over J_f , to see whether a single scalar (Δ) parameterization is useful in the fully two- or three-dimensional case. More broadly, by understanding the time-dependent problem including diffusion, we should be able to reconcile the various theoretical, numerical and observational approaches to bar–halo friction, which is one of the most promising small-scale windows onto the nature of dark matter. An investigation along these lines is underway.

6. Summary

In this paper, we have investigated the impact of diffusion upon the resonant imprints left by rigidly rotating galactic bars in the distribution function (DF) of stars and dark matter particles, and the subsequent effect this has on bar–halo friction. Our key findings can be summarized as follows.

1. Using the pendulum approximation to describe the secular forcing by the bar and assuming a simple diffusion in the associated slow action variable, we proposed a kinetic equation for the DF that depends on just one parameter, the diffusion strength Δ , equal to the ratio of the resonant libration period to the diffusion time across the resonance. Though many classic analytic studies took $\Delta = 0$ by default, Δ can in fact be significantly larger than zero both in real astrophysical systems and in simulations of

supposedly collisionless systems, even if the system's naive relaxation time is a Hubble time or longer.

2. Assuming simple initial/boundary conditions, we solved this kinetic equation for a wide range of Δ values. For $\Delta = 0$ and $t \rightarrow \infty$, we recovered the classic result in which the DF is spread uniformly (“phase-mixed”) along the pendulum Hamiltonian contours in slow angle-action space. This phase-mixed structure was broken for finite Δ , and we provided an analytic understanding of the resulting DF in the $\Delta \ll 1$ and $\Delta \gg 1$ limits.
3. We calculated the corotation torque density \mathcal{S} felt by a galactic bar due to its frictional interaction with an initially spherical halo of dark matter particles, focusing on the contribution from particles orbiting coplanar with the bar, for various Δ . For $\Delta = 0$, we recovered the result of Tremaine & Weinberg (1984) that $\mathcal{S} \rightarrow 0$ as $t \rightarrow \infty$. However, because diffusion replenishes the asymmetry of the DF in the resonant region of phase space, the steady-state torque never vanished for finite Δ . Instead, we found $\mathcal{S} \sim \min(\Delta^{4/5}, 1) \times \mathcal{S}_{\text{LBK}}$, where \mathcal{S}_{LBK} is the (negative) linear theory result from Lynden-Bell & Kalnajs (1972).

Our work highlights the fact that resonant phenomena are delicate, and that one must therefore be mindful of the effects of diffusion if one is to understand how resonances sculpt galaxies. We have shown this for the particular scenario of bar–dark matter halo coupling, but we suspect that analogous conclusions may apply to resonant imprints left in solar neighborhood kinematic data. Further work will be needed to make our rather qualitative claims precise.

Acknowledgments

We are grateful to the referee for a close reading and several suggestions that strengthened our paper considerably. We also thank S. Tremaine, C. Terquem, R. Rafikov, R. Sanderson, M. Weinberg, K. Johnston, B. Kocsis, T. Yavetz, U. Banik, E. Vasiliev, S. Chakrabarti, C. Pichon, A. Bhattacharjee, R. Chiba, L. Beraldo e Silva, and members of the CCA Dynamics group for helpful comments and discussions. This work was supported by a grant from the Simons Foundation (816048, CH), by the U.S. Department of Energy under contract DE-AC02-09CH11466 (VND), by the Institute for Advanced Study (LA), and by the W.M. Keck Foundation Fund at the Institute for Advanced Study (ET). This work was performed in part at Aspen Center for Physics, which is supported by National Science Foundation grant PHY-1607611.

Appendix

Analytic Results for Weak and Strong Diffusion

In this appendix, we derive some analytic results that allow us to understand the solutions to the kinetic Equation (30) in the asymptotic limits of weak diffusion $\Delta \ll 1$ (Appendix A.1) and strong diffusion $\Delta \gg 1$ (Appendix A.2).

A.1. The Limit of Weak Diffusion, $\Delta \ll 1$

A.1.1. Phase-mixed DF in the Collisionless Limit $\Delta = 0$

The (coarse-grained) steady-state phase-mixed DF for $\Delta = 0$ is easily calculated by smearing the initial DF evenly over the phase space contours, as described for example by Binney (2016), Monari et al. (2017), and in a different context by Hamilton (2022). Let us call this phase-mixed DF $f_{\text{pm}}(\phi, j)$; then

we know it will only be a function of h , where

$$h(\phi, j) \equiv \frac{1}{2}j^2 - \cos \phi \quad (\text{A1})$$

is the effective dimensionless Hamiltonian. The initial DF f_{init} (Equation (36)) written in terms of (ϕ, h) is

$$f_{\text{init}} = f_0(0) + \alpha j_{\pm}(\phi, h), \quad (\text{A2})$$

where $j_{\pm} \equiv \pm \sqrt{2(h + \cos \phi)}$ and we take $+$ or $-$ depending on whether we are applying the equation to positive or negative j . Now, for $\Delta = 0$ there are two well-defined orbit families, namely librating ($h < 1$) and circulating ($h > 1$) orbits, distinguished by a separatrix ($h = 1$). Because the resonant island is symmetric around $j = 0$ (e.g., Figure 1), it is geometrically obvious that, for librating orbits, the average phase space density on any given contour is just

$$f_{\text{pm}}^{\text{lib}} = f_0(0), \quad (\text{A3})$$

and hence $g_{\text{pm}}^{\text{lib}} = 0$ (see the final panel of Figure 2(a)). For circulating orbits ($h > 1$), we use the fact that the line element in the (ϕ_*, j_*) plane at fixed h is

$$d\lambda = d\phi_* \sqrt{1 + \frac{\sin^2 \phi_*}{j_{\pm}^2(\phi_*, h)}}. \quad (\text{A4})$$

The phase-mixed DF at fixed $h(\phi, j)$ is then found by averaging (A2) over the contour:

$$f_{\text{pm}}^{\text{circ}}(h(\phi, j)) = f_0(0) + \alpha \frac{\oint d\lambda j_{\pm}(\phi_*, h)}{\oint d\lambda}. \quad (\text{A5})$$

Equations (A3)–(A5) fully describe the phase-mixed DF f_{pm} , toward which the solution to (30) tends in the time-asymptotic limit.

A.1.2. Steady-state DF for Finite Diffusion, $0 < \Delta \ll 1$

When diffusion is finite but weak ($0 < \Delta \ll 1$), the steady-state solution to (30) is modified somewhat from the perfectly phase-mixed solution f_{pm} —see Figure 2(b) and the blue lines in Figures 3(c) and 5. We can gain some insight into this modified steady-state DF following the method of Pao (1988) (see also Petviachvili 1999).

First, we look for a steady-state perturbative solution

$$f_{\text{steady}}(\phi, j) = f_{\text{pm}}(h) + \delta f_{\text{steady}}(\phi, j), \quad (\text{A6})$$

where $|\delta f_{\text{steady}}/f_{\text{pm}}| = \mathcal{O}(\Delta)$. We then have from (30) that

$$j \frac{\partial \delta f_{\text{steady}}}{\partial \phi} - \sin \phi \frac{\partial \delta f_{\text{steady}}}{\partial j} \approx \Delta \frac{\partial^2 f_{\text{pm}}}{\partial j^2}. \quad (\text{A7})$$

To solve this equation, we change variables from $(\phi, j) \rightarrow (\phi, h)$, where h is given in (A1). Then Equation (A7) becomes

$$\frac{\partial \delta f_{\text{steady}}}{\partial \phi} = \Delta \frac{\partial}{\partial h} [j_{\pm}(\phi, h) f_{\text{pm}}'(h)]. \quad (\text{A8})$$

The solution to (A8) is

$$\begin{aligned} \delta f_{\text{steady}}(\phi, h) &= \pm \Delta \frac{\partial}{\partial h} \left[f_{\text{pm}}'(h) \int^{\phi} dx \sqrt{2(h + \cos x)} \right] \\ &= \pm \Delta \frac{\partial}{\partial h} \left[2\sqrt{2(1+h)} f_{\text{pm}}'(h) E\left(\frac{\phi}{2}, \sqrt{\frac{2}{1+h}}\right) \right], \end{aligned} \quad (\text{A9})$$

where $E(\phi, x) \equiv \int_0^{\phi} dy \sqrt{1 - x^2 \sin^2 y}$ is an incomplete elliptic integral of the second kind, and we take $+$ or $-$ depending on whether we apply the equation to $j > 0$ or $j < 0$. For the circulating region of phase space ($h > 1$), we can get an explicit form for $f_{\text{pm}}'(h)$ as follows. We integrate Equation (A8) with respect to ϕ from $-\pi$ to π and get

$$0 = \frac{\partial}{\partial h} \left[4f_{\text{pm}}^{\text{circ}}(h) \sqrt{h-1} E\left(\sqrt{\frac{-2}{h-1}}\right) \right], \quad (\text{A10})$$

where $E(x) \equiv E(\pi/2, x)$ is the complete elliptic integral of the second kind. It follows that the quantity in square brackets is equal to a constant. We can fix this constant by using the fact that, very far from the resonance, we have $h \approx j^2/2 \gg 1$ and f_{pm} is unperturbed, $f_{\text{pm}} \approx f_{\text{init}} = f_0(0) \pm \alpha\sqrt{2h}$ (see Equation (36)).

Then we find that the square bracket is equal to $\pm\pi\sqrt{2}\alpha$, so¹⁶

$$f_{\text{pm}}^{\text{circ}}(h) = \frac{\sqrt{2}\pi\alpha}{4\sqrt{h-1}} \left[E\left(\sqrt{\frac{-2}{h-1}}\right) \right]^{-1}. \quad (\text{A11})$$

Combining this with (A9), we have that, for $h > 1$,

$$\begin{aligned} \delta f_{\text{steady}}^{\text{circ}}(\phi, h) &= \pm \alpha \Delta \pi \frac{\partial}{\partial h} \left[\sqrt{\frac{h+1}{h-1}} \frac{E(\phi/2, \sqrt{2/[1+h]})}{E(\sqrt{-2/[h-1]})} \right]. \end{aligned} \quad (\text{A12})$$

Though we do not illustrate it here, Equation (A12) does a fairly good job of reproducing the numerical solution for the region $|j| > 2$. On the other hand, when we apply the same solution technique to the librating portion of phase space ($h < 1$), it fails. The reason is that $f_{\text{pm}}^{\text{lib}}(h) = \text{constant}$ (see Equation (A3)) so that $f_{\text{pm}}^{\text{lib}}(h) = 0$, and hence (A9) would predict $\delta f_{\text{steady}}^{\text{lib}} = 0$. This a poor solution, as can be seen by inspecting Figure 2(b). Of particular importance for dynamical friction calculations (Section 4) is the fact that this solution fails to reproduce the major contributions to the $\text{Im } g_1$ curve for $|j| < 2$ shown for small Δ in Figure 5.

The reason for the failure of this solution is that, for small Δ , sharp gradients in the DF tend to build up near the separatrix, meaning that the term $\Delta \partial^2 \delta f_{\text{steady}} / \partial j^2$ on the right-hand side of Equation (30) cannot be neglected—the approximation (A7) therefore breaks down. To remedy this, one can treat the region near the separatrix as a boundary layer where δf_{steady} can be of the same order as f_{pm} . The reader is referred to Pao (1988) for details of how this calculation works, although in practice it is a cumbersome task and the final expressions are rather unenlightening. The important point is that one gets an

additional skew-symmetric contribution to the DF (in the sense of (39)) in a layer on the inner edge of the separatrix, which is of the same order as the phase-mixed solution f_{pm} . The thickness of the layer grows with Δ , although not in a way that is easily quantified; empirically, this leads to the low- Δ behavior described in Section 3.2, and in particular to the approximate scaling $\max(\text{Im } g_1) \propto \Delta^{4/5}$ (Figure 6(b)).

A.2. The Limit of Strong Diffusion, $\Delta \gg 1$

Let us now consider the opposite limit, in which the timescale for diffusion t_{diff} is short compared to the libration time t_{lib} , i.e., $\Delta \gg 1$. We note that the initial DF (36) is annihilated by the collision operator on the right-hand side of (30) because $\Delta \partial^2 f_{\text{init}}(j) / \partial j^2 = 0$. Thus, in the limit of infinitely strong diffusion $\Delta \rightarrow \infty$, when this term is the dominant one in the kinetic equation, we expect that the solution $f(\phi, j, \tau)$ will never deviate from f_{init} . Therefore, without loss of generality, let us write

$$f(\phi, j, \tau) = f_{\text{init}}(j) + \delta f(\phi, j, \tau). \quad (\text{A13})$$

Plugging this into the kinetic Equation (30), we find

$$\frac{\partial \delta f}{\partial \tau} + j \frac{\partial \delta f}{\partial \phi} - \sin \phi \left(\alpha + \frac{\partial \delta f}{\partial j} \right) = \Delta \frac{\partial^2 \delta f}{\partial j^2}. \quad (\text{A14})$$

For large but finite diffusion, $\Delta \gg 1$, we anticipate that δf will be finite but small (see Figure 2(d)), so that $\epsilon(\phi, j) \equiv |(\partial \delta f / \partial j) / \alpha| \ll 1$ is small. Our aim in this section will be to compute δf to lowest order in this small parameter. Higher-order solutions are also possible (Duarte et al. 2019), but they will not be necessary for our purposes. Let us therefore drop the term $\partial \delta f / \partial j$ from (A14) and write

$$\frac{\partial \delta f}{\partial \tau} + j \frac{\partial \delta f}{\partial \phi} - \alpha \sin \phi \approx \Delta \frac{\partial^2 \delta f}{\partial j^2}. \quad (\text{A15})$$

We now take advantage of the periodicity of the coordinate system to expand δf as a Fourier series: $\delta f(\phi, j, \tau) = \sum_{n=-\infty}^{\infty} \delta f_n(j, \tau) \exp(in\phi)$. Since f is real, we must have $\delta f_n^*(j, \tau) = \delta f_{-n}(j, \tau)$. Plugging the Fourier expansion into (A15) and using the orthogonality of Fourier harmonics, we get

$$\frac{\partial \delta f_n}{\partial \tau} + inj \delta f_n + \frac{i\alpha}{2} (\delta_{n-1}^0 - \delta_{n+1}^0) = \Delta \frac{\partial^2 \delta f_n}{\partial j^2}. \quad (\text{A16})$$

The solution to this equation is $\delta f_n = 0$ for $n \neq \pm 1$, while for $n = \pm 1$ we have:

$$\delta f_{\pm 1}(j, \tau) = \pm \frac{\alpha}{2i\Delta^{1/3}} \int_0^{\Delta^{1/3}\tau} dy \exp\left(-\frac{y^3}{3} \mp \frac{ijy}{\Delta^{1/3}}\right). \quad (\text{A17})$$

It follows that the solution to the kinetic Equation (30) for $\Delta \gg 1$ is approximately

$$\begin{aligned} f(\phi, j, \tau) &= f_{\text{init}}(j) + \frac{\alpha}{\Delta^{1/3}} \int_0^{\Delta^{1/3}\tau} dy \sin\left(\phi - \frac{jy}{\Delta^{1/3}}\right) \exp\left(-\frac{y^3}{3}\right). \end{aligned} \quad (\text{A18})$$

The $\exp(-y^3/3)$ factor in the integrand of (A18) means that the contribution to the integral from y values $\gtrsim 2$ is negligible,

¹⁶ Of course, one can also derive an exact expression for $f_{\text{pm}}^{\text{circ}}(h)$ by differentiating the phase-mixed solution (A5), but the approximate expression (A11) is simpler and sufficiently accurate for our purposes.

meaning the steady state is approximately reached when $\tau \sim \Delta^{-1/3}$.

We note also that, in this limit, we get an explicit expression for the key quantity $\text{Im}f_1$ in steady state:

$$\text{Im}f_1(j, \tau \rightarrow \infty) = \frac{\alpha}{2\Delta^{1/3}} \int_0^\infty dy \exp\left(-\frac{y^3}{3}\right) \cos\left(\frac{jy}{\Delta^{1/3}}\right), \quad (\text{A19})$$





which leads directly to Equations (46)–(47).

Finally, we can use the solution (A18) to check our assumption that $\epsilon \equiv |(\partial\delta f/\partial j)/\alpha| \ll 1$. We take the derivative of $f - f_{\text{init}}$ with respect to j and divide by α to find

$$\begin{aligned} \epsilon &\approx \Delta^{-2/3} \left| \int_0^\infty dy y \sin\left(\phi - \frac{jy}{\Delta^{1/3}}\right) \exp\left(-\frac{y^3}{3}\right) \right| \\ &\leq \Delta^{-2/3} \left| \int_0^\infty dy y \exp\left(-\frac{y^3}{3}\right) \right| \approx 0.94 \Delta^{-2/3}. \end{aligned} \quad (\text{A20})$$

Thus, ϵ is small as long as $\Delta \gtrsim$ a few.

ORCID iDs

Chris Hamilton  <https://orcid.org/0000-0002-5861-5687>
 Elizabeth A. Tolman  <https://orcid.org/0000-0002-2642-064X>
 Lev Arzamasskiy  <https://orcid.org/0000-0002-5263-9274>
 Vinícius N. Duarte  <https://orcid.org/0000-0001-8096-7518>

References

- Antoja, T., Helmi, A., Dehnen, W., et al. 2014, *A&A*, **563**, A60
 Athanassoula, E. 2003, *MNRAS*, **341**, 1179
 Athanassoula, E. 2013, *Secular Evolution of Galaxies* (Cambridge: Cambridge Univ. Press), 305
 Auerbach, S. P. 1977, *PhFI*, **20**, 1836
 Banik, U., & van den Bosch, F. C. 2021, *ApJ*, **912**, 43
 Banik, U., & van den Bosch, F. C. 2022, *ApJ*, **926**, 215
 Bar-Or, B., Fouvry, J.-B., & Tremaine, S. 2019, *ApJ*, **871**, 28
 Beraldo e Silva, L., de Siqueira Pedra, W., & Valluri, M. 2019, *ApJ*, **872**, 20
 Berk, H. L., & Breizman, B. N. 1998, Overview of nonlinear theory of kinetically driven instabilities, Tech. Rep.DOE/ER/54346-841, Univ. Texas, Inst. for Fusion Studies Overview of nonlinear theory of kinetically driven instabilities, Tech. Rep.
 Berk, H. L., Breizman, B. N., & Pekker, M. 1996, *PhRvL*, **76**, 1256
 Berk, H. L., Breizman, B. N., & Pekker, M. 1997, *PlPhR*, **23**, 778
 Binney, J. 2012, *MNRAS*, **426**, 1324
 Binney, J. 2013, *NewAR*, **57**, 29
 Binney, J. 2016, *MNRAS*, **462**, 2792
 Binney, J. 2018, *MNRAS*, **474**, 2706
 Binney, J. 2020a, *MNRAS*, **495**, 895
 Binney, J. 2020b, *MNRAS*, **495**, 886
 Binney, J., & Lacey, C. 1988, *MNRAS*, **230**, 597
 Binney, J., & Tremaine, S. 2008, *Galactic Dynamics: Second Edition* (Princeton, NJ: Princeton Univ. Press)
 Black, C., Germaschewski, K., Ng, C. S., & Bhattacharjee, A. 2008, BAPS, 53, GP6.00066, <http://meetings.aps.org/link/BAPS.2008.DPP.GP6.66>
 Brodin, G. 1997, *PhRvL*, **78**, 1263
 Buta, R. 1986, *ApJS*, **61**, 609
 Buta, R. J. 2017, *MNRAS*, **470**, 3819
 Callen, J. D. 2014, *PhPl*, **21**, 052106
 Catto, P. J. 2020, *JPhI*, **86**, 815860302
 Catto, P. J., & Tolman, E. A. 2021, *JPhI*, **87**, 905870309
 Chiba, R., Friske, J. K. S., & Schönrich, R. 2020, *MNRAS*, **500**, 4710
 Chiba, R., & Schönrich, R. 2021, *MNRAS*, **505**, 2412
 Chiba, R., & Schönrich, R. 2022, *MNRAS*, **513**, 768
 Chirikov, B. V. 1979, *PhR*, **52**, 263
 Collier, A., & Madigan, A.-M. 2021, *ApJ*, **915**, 23
 Daniel, K. J., Schaffner, D. A., McCluskey, F., Fiedler Kawaguchi, C., & Loebman, S. 2019, *ApJ*, **882**, 111
 De Simone, R., Wu, X., & Tremaine, S. 2004, *MNRAS*, **350**, 627
 Debattista, V. P., & Sellwood, J. A. 1998, *ApJ*, **493**, L5
 Debattista, V. P., & Sellwood, J. A. 2000, *ApJ*, **543**, 704
 Dehnen, W. 2000, *AJ*, **119**, 800
 Dootson, D., & Magorrian, J. 2022, arXiv:2205.15725
 Duarte, V. N., & Gorenkov, N. N. 2019, *NucFu*, **59**, 044003
 Duarte, V. N., Gorenkov, N. N., White, R. B., & Berk, H. L. 2019, *PhPl*, **26**, 120701
 Duarte, V. N., Lestz, J. B., Gorenkov, N. N., & White, R. B. 2023, *PhRvL*, **130**, 105101
 Dupree, T. H. 1966, *PhFI*, **9**, 1773
 El-Zant, A. A., Freundlich, J., Combes, F., & Halle, A. 2020, *MNRAS*, **492**, 877
 Fouvry, J.-B., & Bar-Or, B. 2018, *MNRAS*, **481**, 4566
 Fouvry, J. B., Pichon, C., Magorrian, J., & Chavanis, P. H. 2015, *A&A*, **584**, A129
 Fragkoudi, F., Grand, R. J., Pakmor, R., et al. 2021, *A&A*, **650**, L16
 Frankel, N., Pillepich, A., Rix, H.-W., et al. 2022, *ApJ*, **940**, 61
 Frankel, N., Sanders, J., Ting, Y.-S., & Rix, H.-W. 2020, *ApJ*, **896**, 15
 Fujii, M. S., Bédorf, J., Baba, J., & Portegies Zwart, S. 2018, *MNRAS*, **482**, 1983
 Hamilton, C. 2022, *ApJL*, **929**, L29
 Hernquist, L. 1990, *ApJ*, **356**, 390
 Hernquist, L., & Weinberg, M. D. 1992, *ApJ*, **400**, 80
 Hilmi, T., Minchev, I., Buck, T., et al. 2020, *MNRAS*, **497**, 933
 Hui, L., Ostriker, J. P., Tremaine, S., & Witten, E. 2017, *PhRvD*, **95**, 043541
 Hunt, J. A. S., Bub, M. W., Bovy, J., et al. 2019, *MNRAS*, **490**, 1026
 Ichimaru, S. 1965, *PhRv*, **140**, 226
 Jenkins, A., & Binney, J. 1990, *MNRAS*, **245**, 305
 Johnston, G. L. 1971, *PhFI*, **14**, 2719
 Kaasalainen, M. 1994, *MNRAS*, **268**, 1041
 Kaufman, A. N. 1972, *JPhI*, **8**, 1
 Kaur, K., & Sridhar, S. 2018, *ApJ*, **868**, 134
 Kaur, K., & Stone, N. C. 2022, *MNRAS*, **515**, 407
 Kawata, D., Baba, J., Hunt, J. A. S., et al. 2021, *MNRAS*, **508**, 728
 Krishnarao, D., Pace, Z. J., D'Onghia, E., et al. 2022, *ApJ*, **929**, 112
 Lancaster, L., Giovanetti, C., Mocz, P., et al. 2020, *JCAP*, **2020**, 001
 Landau, L. D. 1946, *Zh. Eksp. Teor. Fiz.*, **10**, 25
 Li, X., Shlosman, I., Heller, C., & Pfenniger, D. 2022, arXiv:2211.04484
 Lichtenberg, A. J., & Lieberman, M. A. 2013, *Regular and Chaotic Dynamics*, Vol. 38 (New York: Springer Science Business Media)
 Lieb, E., Collier, A., & Madigan, A.-M. 2021, *MNRAS*, **509**, 685
 Ludlow, A. D., Fall, S. M., Schaye, J., & Obreschkow, D. 2021, *MNRAS*, **508**, 5114
 Ludlow, A. D., Schaye, J., & Bower, R. 2019, *MNRAS*, **488**, 3663
 Lynden-Bell, D., & Kalnajs, A. J. 1972, *MNRAS*, **157**, 1
 Mackereth, J. T., Bovy, J., Leung, H. W., et al. 2019, *MNRAS*, **489**, 176
 Mazitov, R. K. 1965, *JAMTP*, **6**, 22
 Minchev, I., & Famaey, B. 2010, *ApJ*, **722**, 112
 Minchev, I., Famaey, B., Quillen, A. C., et al. 2012, *A&A*, **548**, A127
 Monari, G., Famaey, B., Fouvry, J.-B., & Binney, J. 2017, *MNRAS*, **471**, 4314
 Monari, G., Famaey, B., Siebert, A., et al. 2016, *MNRAS*, **465**, 1443
 Monari, G., Famaey, B., Siebert, A., Wegg, C., & Gerhard, O. 2019, *A&A*, **626**, A41
 Nelson, R. W., & Tremaine, S. 1999, *MNRAS*, **306**, 1
 Ng, C. S., Bhattacharjee, A., & Skiff, F. 2006, *PhPl*, **13**, 055903
 O'Neil, T. 1965, *PhFI*, **8**, 2255
 Palmer, P. L., & Papaloizou, J. 1987, *MNRAS*, **224**, 1043
 Pao, Y. 1988, *PhFI*, **31**, 302
 Peñarrubia, J. 2019, *MNRAS*, **490**, 1044
 Petviachvili, N. 1999, PhD thesis, Univ. Texas Austin
 Pichon, C., & Aubert, D. 2006, *MNRAS*, **368**, 1657
 Roshan, M., Ghafourian, N., Kashfi, T., et al. 2021, *MNRAS*, **508**, 926
 Roškar, R., Debattista, V. P., Quinn, T. R., Stinson, G. S., & Wadsley, J. 2008, *ApJL*, **684**, L79
 Rozier, S. 2020, PhD thesis, Sorbonne Université
 Rozier, S., Fouvry, J.-B., Breen, P. G., et al. 2019, *MNRAS*, **487**, 711
 Schönrich, R., & Binney, J. 2009, *MNRAS*, **396**, 203
 Sellwood, J. 2008, *ApJ*, **679**, 379
 Sellwood, J., & Debattista, V. P. 2006, *ApJ*, **639**, 868
 Sellwood, J. A. 2012, *ApJ*, **751**, 44
 Sellwood, J. A. 2013, *ApJL*, **769**, L24
 Sellwood, J. A. 2014, *RvMP*, **86**, 1
 Sellwood, J. A., & Binney, J. J. 2002, *MNRAS*, **336**, 785

- Sellwood, J. A., & Debattista, V. P. 2009, [MNRAS](#), **398**, 1279
- Sellwood, J. A., Trick, W. H., Carlberg, R. G., Coronado, J., & Rix, H.-W. 2019, [MNRAS](#), **484**, 3154
- Sridhar, S. 2019, [ApJ](#), **884**, 3
- Su, C. H., & Oberman, C. 1968, [PhRvL](#), **20**, 427
- Ting, Y.-S., & Rix, H.-W. 2019, [ApJ](#), **878**, 21
- Tolman, E. A., & Catto, P. J. 2021, [JPIPh](#), **87**, 855870201
- Tremaine, S., & Weinberg, M. D. 1984, [MNRAS](#), **209**, 729
- Trick, W. H. 2021, [MNRAS](#), **509**, 844
- Trick, W. H., Coronado, J., & Rix, H.-W. 2019, [MNRAS](#), **484**, 3291
- Weinberg, M. D. 1985, [MNRAS](#), **213**, 451
- Weinberg, M. D. 1989, [MNRAS](#), **239**, 549
- Weinberg, M. D. 1994, [ApJ](#), **420**, 597
- Weinberg, M. D. 2001, [MNRAS](#), **328**, 311
- Weinberg, M. D. 2004, [arXiv:astro-ph/0404169](#)
- Weinberg, M. D., & Katz, N. 2007a, [MNRAS](#), **375**, 425
- Weinberg, M. D., & Katz, N. 2007b, [MNRAS](#), **375**, 460
- White, R. B., & Duarte, V. N. 2019, [PhPI](#), **26**, 042512
- Wilkinson, M. J., Ludlow, A. D., Lagos, C. d. P., et al. 2023, [MNRAS](#), **519**, 5942
- Wu, Y.-T., Pfenniger, D., & Taam, R. E. 2016, [ApJ](#), **830**, 111
- Yavetz, T. D., Johnston, K. V., Pearson, S., Price-Whelan, A. M., & Weinberg, M. D. 2020, [MNRAS](#), **501**, 1791
- Zakharov, V. E., & Karpman, V. I. 1963, [JETP](#), **16**, 351